MODELING CATALYST ACTIVITY AND SELECTIVITY FOR THE GAS TO LIQUID TECHNOLOGY (GTL)

A Thesis

by

NOSAIBA ABDELMAGID ELTAYEB MOHAMED

Submitted to the Office of Graduate and Professional Studies of
Texas A&M University
in partial fulfillment of the requirements for the degree of

MASTER OF SCIENCE

Chair of Committee,	Nimir O. Elbashir
Co-Chair of Committee,	Patrick Linke
Committee Member,	Haitham Abu-Rub
Head of Department,	Arul Jayaraman

December 2019

Major Subject: Chemical Engineering

ABSTRACT

The activity and selectivity of catalytic systems used in gas to liquid (GTL) technology have been studied. In the activity study, seven catalytic systems that were used in the dry reforming of methane have been analyzed. The generalized power law expression (GPLE) model was used to fit the activity profile and predict mechanism of catalyst deactivation. The first and second order GPLE fit well to the experimental data with regression factor (R^2) ranged between 0.95 and 0.99. Also, it was possible to deconvolute the deactivation mechanism into two main causes, fast deactivation by sintering and the slow deactivation by carbon deposition.

In the selectivity study, a detailed kinetics model was developed to estimate the product distribution of the cobalt catalyst in the supercritical fluid phase of the Fischer-Tropsch synthesis reaction (SCF-FTS) up to carbon number 15. The adopted mechanism to describe the reaction network is the alkyl mechanism. Six experimental runs were conducted, corresponding to three temperature levels of experimental data (230℃, 240℃ and 250℃), three total pressures (45 bar, 65 bar, and 80 bar) to capture the critical and near critical condition, (H_2:CO=2:1) and gas hourly space velocity (GHSV) of 500 (1/h). To estimate the model parameters a genetic algorithm code was developed in MATLAB. The model results showed that the maximum mean absolute relative residual (MARR) was 35.32%. Moreover, the model was able to predict the n-paraffin formation rate and Anderson-Schulz-Flory (ASF) product distribution with acceptable range of error.

DEDICATION

This thesis is dedicated to the spirit of the martyrs of the glorious December 2018 revolution in Sudan

ACKNOWLEDGEMENTS

I would like to express my sincere gratitude and thankfulness to my advisor, Dr. Nimir Elbashir, and my committee members, Dr. Patrick Linke, and Dr. Haitham Abu-Rub, for their guidance and support throughout the course of this research.

I would also like to thank Dr. Hanif Choudhury for his unlimited support as well as for his assistance in running the experimental campaign. I am also grateful to Mohamed Sufiyan Challiwala and Shaik Afzal for their helpful discussion and assistance in the developing of kinetic model and genetic algorithm code. I also extend my gratitude to all the members of our research group for their valuable scientific discussions and for sharing their experimental data.

Thanks also go to my friends and colleagues and the department faculty and staff for making my time at Texas A&M University at Qatar a great experience. Finally, thanks to my parents for their encouragement and to my husband and my son for their patience and love.

CONTRIBUTORS AND FUNDING SOURCES

Contributors

This work was supervised by a thesis committee consisting of Professor Nimir Elbashir and Patrick Linke from the Department of Chemical Engineering and Professor Haitham Abu-Rub from the Department of Electrical Engineering.

The experimental campaign for supercritical Fischer-Tropsch was done in Professor Elbashir's lab at Texas A&M University at Qatar and with the help of Dr. Hanif Choudhury and Mr. Mohamed Sufiyan Challiwala. The experimental data for the bimetallic and monometallic catalyst was provided from Dr. Anjaneyulu Chatla. The catalyst activity data for the Riogen and the ALD catalyst was provided from Mr. Shaik Afzal and Mr. Anuj Varghese Prakash.

All other work conducted for the thesis was completed by the student independently.

Funding Sources

Graduate study was supported by a fellowship from Texas A&M University at Qatar.

This work was also made possible in part by a grant from Qatar National Research Fund (QNRF) under Grant Number (7-865-2-320) and NPRP exceptional grant award [NPRP-EP X-100-2-024].

NOMENCLATURE

8WVS	Eight Way Selecting Valve
A	Pre-Exponential Factor in Arrhenius Rate Equation
AG	Air Generator
ALD	Atomic Layer Deposition
ATR	Autothermal Reforming
Al_2O_3	Alumina
Ar	Argon
ASF	Anderson-Schulz-Flory
BPR	Backpressure Regulator
CH_4	Methane
Co	Cobalt
CO	Carbon monoxide
CO_2	Carbon dioxide
CV	The Percent of Vacant Sites
DRM	Dry Reforming of Methane
ESDV	Emergency Shutdown Valve
FBR	Fluidized Bed Reactors
Fe	Iron
FID	Flame Ionization Detector
FTS	Fischer-Tropsch Synthesis

FP	Feed Purification
GC	Gas Chromatograph
GTL	Gas-to-Liquid
GHG	Green House Gases
GHSV	Gas Hourly Space Velocity
GPLE	General Power Low Expression
H_2	Hydrogen
H_2O	water
He	Helium
HPLC	High-Pressure Liquid Pump
LH	Langmuir-Hinshelwood
LHHW	Langmuir-Hinshelwood-Hougen-Waston
MARR	Mean Absolute Relative Residual
MFC	Mass Flow Controller
MS	Mass Spectroscopy
NG	Natural Gas
N_2	Nitrogen
Ni	Nickel
NRV	Non-Return Valve
PCV	Pressure Control Valve
PI	Pressure Indicator
PPE	Personal Protective Equipment

PSV	Pressure Safety Valve
PT	Pressure Transmitter
PV	Pressure Valve
POX	Partial Oxidation
PLE	Power Law Expression
QNRF	Qatar National Research Fund
QP	Qatar Petroleum
RDS	Rate Determine Step
Ru	Ruthenium
RWGS	Reverse Water Gas Shift
SC	Supercritical
SCF	Supercritical Fluids
SC-FTS	Supercritical Fischer-Tropsch Synthesis
SM	Static Mixer
SPR	Slurry Phase Reactors
SRM	Steam Reforming of Methane
SSA	Steady State Activity
TAMUQ	Texas A&M University at Qatar
TCD	Thermal Conductivity Detector
TFBR	Tubular Fixed Bed Reactors
V	Vessel
WGS	Water Gas Shift

α	The Chain Growth Probability
γ_j	The Activity Coefficient of Component i
δ	The Solubility Parameter
ϕ	The Volume Fraction
v	The Molar Volume
ΔE	Activation Energy
ΔH	Heat of Reaction / Adsorption (As Applicable)

TABLE OF CONTENTS

Page

LIST OF FIGURES

Page

LIST OF TABLES

Page

1. INTRODUCTION AND LITERATURE REVIEW

Natural gas (NG) become one of the primary energy sources as the clean fossil fuel. In 2012, the utilization of natural gas as an energy source was 23.9% of the total energy consumption, and it was primarily used for power generation, heating, and industry. Most of this gas is supplied to the ultimate consumer by pipeline distribution. The demand for gas transportation is subject to future uncertainties and logistical constraints [1]. As the future demand for energy is expected to increase, traditional sources of energy must be utilized more efficiently and sustainable. Gas-to-Liquid (GTL) Technology has become an important technology in converting natural gas to ultra-clean fuels and value-added chemicals. GTL has been considered a favorable route for the utilization of natural gas, and it starts with the reforming of natural gas or methane to produce syntheses gas (or syngas, a mixture of carbon monoxide (CO) and hydrogen (H_2)), followed by the Fischer Tropsch synthesis (FTS) process that converts this syngas into value-added chemicals and environmentally attractive fuels [2].

Qatar owns the third world largest natural gas reserves. In 2006 and 2011, Qatar commercialized the ORYX GTL in collaboration with Sasol and the Pearl GTLK Plant in collaboration with Shell, respectively. The Pearl GTL plant is the world largest plant and it represents cutting-edge operation for GTL commercial scale production [1].

GTL technology involves three main steps: (1) production of the syngas via methane reforming, (2) formation of liquid hydrocarbons and condensates via the Fischer-Tropsch synthesis (FTS) technology and finally (3) the refining and fractionation of the

hydrocarbon products in form of fuel cuts and the value-added chemicals [3]. A simplified block flow diagram of the GTL process is shown in Figure 1.

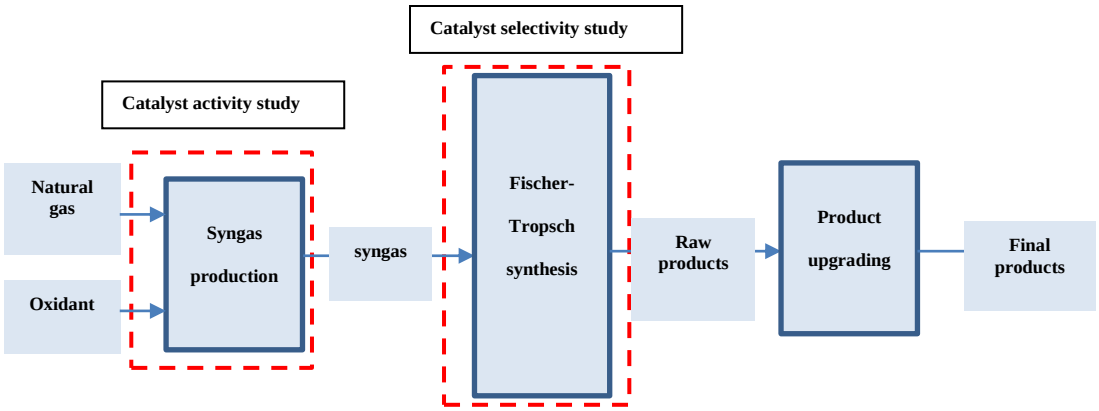

Figure 1: General description of the GTL process stages

1.1. Synthesis Gas Production

The most expensive unit in the GTL plant is the syngas production unit, which is account for 50 - 75% of the total cost of the GTL complex [4]. In this unit the methane is converted to a mixture of carbon monoxide (CO) and hydrogen (H_2) with different molar ratio depending on the type of reformer. There are several different reforming techniques utilized in the GTL plants based on the way of the oxidation of the methane, but the most common are: the steam reforming (SRM), the partial oxidation (POX), the autothermal reforming (ATR), and the dry reforming of methane (DRM). Most of these reforming techniques use a heterogeneous catalyst to improve the process.

The most common commercial reforming technology is the SRM. The reaction is highly endothermic and combined with water-gas shift reaction to produce a syngas with (H_2:CO) ratio of ≥ 3.

$$CH_4 + H_2O \rightarrow CO + 3H_2 \qquad \Delta H^{\circ}_{298K} = 206 \frac{kJ}{mol} \qquad \text{Eq.1}$$

$$CO + H_2O \rightarrow CO_2 + H_2 \qquad \Delta H^{\circ}_{298K} = 163 \frac{kJ}{mol} \qquad \text{Eq.2}$$

In the contrast, POX reforming technology is an exothermic reaction that can be run catalytically or non-catalytically. The reforming process happened by the partial combustion of the natural gas and oxygen. In the non-catalytic partial oxidation, the reaction required high operating temperature and pressure (1200-1500 C^o and 58-80 bar) while in the catalytic partial oxidation the reaction operating temperature is lower (800-900 C^o). The produced syngas has (H_2:CO) ratio about 2, which is the ratio required for the FTS. Nevertheless, POX require pure oxygen that come from the costly Air Separation Unit (ASU) and the reaction proceeds as follows:

$$CH_4 + \frac{1}{2}O_2 \rightarrow CO + 2H_2 \qquad \Delta H^{\circ}_{298K} = -32 \frac{kJ}{mol} \qquad \text{Eq.3}$$

$$CH_4 + 2O_2 \rightarrow CO_2 + 2H_2O \qquad \Delta H^{\circ}_{298K} = -802 \frac{kJ}{mol} \qquad \text{Eq.4}$$

The ATR of the methane is a combination of the SRM and POX work together to reduce the temperature required in the reaction and to increase the hydrocarbon conversion. The ATR reactor consists of combustion chamber at the top followed by catalytic bed at the bottom. The methane premixed with the oxygen and the steam before ignited in the combustion chamber. The combustion influences flow through the catalyst bed and exit close to equilibrium conversion and the produced syngas has (H_2:CO) ratio about 2.5.

The DRM gained a great attention lately since it uses two of the greenhouse gases (GHG) (methane and carbon monoxide) to produce the synthesis gas. The DRM is an endothermic process that consists of a main reaction to produce the synthesis gas and three

side reaction (Boudouard reaction, Methane decomposition and Reverse Water Gas shift (RWGS) reaction).

Main reaction: $CH_4 + CO_2 \rightarrow 2CO + 2H_2$ $\Delta H^{\circ}_{298K} = 247 \frac{kJ}{mol}$ Eq.5

Methane decomposition: $CH_4 \leftrightarrow C + 2H_2$ $\Delta H^{\circ}_{298K} = 75 \frac{kJ}{mol}$ Eq.6

Boudouard reaction: $2CO \leftrightarrow CO_2 + C$ $\Delta H^{\circ}_{298K} = -171 \frac{kJ}{mol}$ Eq.7

Reverse Water Gas shift (RWGS) reaction): $CO_2 + H_2 \rightarrow CO + H_2O$ $\Delta H^{\circ}_{298K} = \frac{41kJ}{mol}$ Eq.8

The produced synthesis gas has (H_2:CO) ratio around unity which may not be suitable for conventional Fischer-Tropsch that requires syngas ratio of ~2. Post treatment of DRM syngas to boost syngas ratio may be required as discussed by [5]. However, using direct low H_2/CO ratio syngas from DRM can also be used to produce olefin rich liquid hydrocarbons [6].

One of the main concerns in Qatar National vision 2030 is to reduce the GHG emission [7]. To do that Qatar is investing to find more effective solutions to reduce the environmental pollution while expanding the energy supply. The DRM technology presents a prospective solution to reduce the GHG. The main problem related to the DRM is the low-quality syngas (H_2:CO=1) and catalyst deactivation. The catalyst deactivation arises due to the multiple sources of the carbon in the process, which lead to accumulate of the carbon on the catalyst services.

1.2. Catalyst Deactivation on the DRM

There are many different catalysts system that can be used for the DRM reaction, such as transition and noble metals. The active transition metals (nickel (Ni) and cobalt (Co)) are generally used as catalyst in the DRM due to their higher activity, availability and low price. On the other hand, the noble metals (platinum, rhodium, palladium, ruthenium and iridium) have significant coke formation resistance and higher activity, but they are more expensive [8]. Accordingly, the active transition metals are more favorable in the DRM reaction. Among the transition metals the Ni-based catalysts are the most popular and are commonly used in the industry.

The catalyst deactivate during the DRM reaction mainly due to coke formation, sintering of the active metal and oxidation of metallic active sites [9]. These deactivation mechanisms can be classified into thermal deactivation (sintering), chemical deactivation (oxidation of metallic active sides) and mechanical deactivation (fouling). The deactivation by sintering (Figure 2) is usually happens in the high temperature processes (higher than 500 ^{o}C) and it is mainly from the loss of the surface area of the catalyst or the support. Since the DRM reaction is normally operates at high temperature ($\geq$800 ^{o}C) and the Ni catalyst crystals has low thermal stability the deactivation by sintering is common in the DRM reaction.

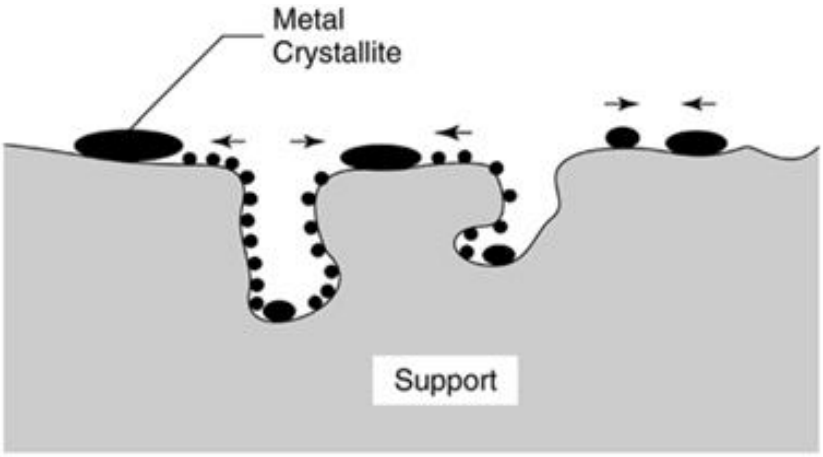

Figure 2: Catalyst deactivation by sintering. Reprinted with permission from[10]

The deactivation by carbon deposition (Figure 3) is mainly occur because of the accumulation of the carbon on the catalyst surface. The carbon aggregations prevent the reactants from accessing the active metal surface inside the pores. In the DRM reaction two side reactions (Boudouard reaction and Methane decomposition) produce carbon which is arise the deactivation by carbon deposition.

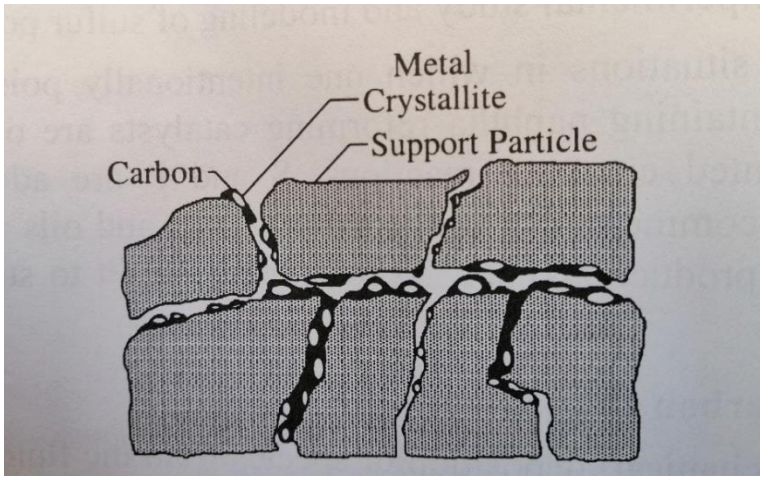

Figure 3:Catalyst deactivation by carbon deposition. Reprinted with permission from [10]

Modelling of the catalyst deactivation process is essential in providing the needed information to design efficient catalyst and to identity the suitable operating conditions

that decrease the rate of deactivation. Also, success in developing accurate deactivation models will save a lot of money compared to the experimental investigations.

1.3. Literature Review on Modeling Catalyst Deactivation Mechanism

Numerous studies over the past several years focused on the study of the catalyst deactivation in DRM reaction. A recent review by Fu et al. [11] focused on using micro kinetic model based on Gibbs energy minimization to identify the deactivation mechanism and the favorable reaction routes for carbon deposition in the DRM reaction using Ni as catalyst. They found that the carbon deposition increases dramatically when the temperature increases more than 650 ^{o}C onwards. Banisharifdehkordi and Baghalha [12] studied the performance and the deactivation of the catalyst in Midrex® industrial fixed bed reactor under combined DRM and SRM reaction using a one-dimensional heterogeneous model. The results showed that there is strong tendency for the catalyst to deactivate by the methane decomposition and the deactivation happened layer by layer inside the catalyst bed. Moreover, they investigated the change in the catalyst size using the X-ray diffraction and they found that over the 41-month operation period the Ni/γ-Al_2O_3 catalyst size increase from 2.445 nm to 9.77 nm. Bartholomew [13] studied the sintering kinetics of the supported metals using the General Power Low Expression (GPLE). He used the dispersion versus time-on-stream (TOS) data of different catalytic systems and fitted to first and second order GPLE. The GPLE was able to relate how the sintering rate can be affect by the temperature, atmosphere, promoter, and support.

Azarpour and Wan Alwi [14] predicted the catalyst deactivation rate of the industrial palladium supported on carbon (Pd/C) catalyst using the first principle model (FPM) and

the process data. They used the GPLE to account for the catalyst deactivation by sintering. Finally, they used the Matlab 2013a environment to solve the material balance equations. The model was able to predict the sintering deactivation rate with less than 3% error.

Pawar et al. [15] studied the short-term catalyst deactivation on the biogas dry reforming using supported Ni catalyst. They used the characterization techniques (XRD, TGA, FTIR and Raman spectroscopies) of the spend catalyst and collected carbon to identify the optimum operation conditions (temperature and CH_4 /CO_2 ratio) to avoid carbon deposition.

Choudhury et al. [16] investigated the catalyst deactivation in FTS reaction under conventional and nonconventional reaction media using packed bed (PB) and Microfibrous Entrapped Cobalt (MFEC) Catalyst bed. They used the GPLE model to predict the catalyst deactivation. The modelling results showed that the MFEC in SCF has more stable performance than the PB in gas phase or SCF. Also, the characterization techniques (chemisorption TEM, and TGA) confirmed the modelling results.

Zhao et al. [17] studied the effect of using atomic layer deposition (ALD) of pours Al_2O_3 on the Ni/γ-Al_2O_3 catalyst for the DRM reaction. They noticed that using of the ALD catalyst suppress the catalyst deactivation by sintering.

From the previous listed review of the catalyst deactivation on the DRM reaction, it is understandable that modelling of the catalyst deactivation is not fully addressed and specifically in terms of quantifying its impact on the catalyst performance. This study is aiming at evaluating the catalyst deactivation mechanism of the DRM reaction using the GPLE method. The unique feature of this method is that it calculates the deactivation rate

of the catalyst and it can give a hint about the type of the deactivation process taking place on the catalyst surface.

1.4. The Fischer-Tropsch Synthesis (FTS)

FTS is the heart of the GTL technology since it is the process responsible for converting syngas into liquid hydrocarbons over the surface of a metal catalyst [18]. FTS is an exothermic polymerization reaction in which CO and H_2 chemically adsorb on the catalyst active site, disassociate and form carbon-hydrogen monomer that go into series of propagation reactions to form chain of hydrocarbons and water (see Eq. 9). Hence, the heat produced from the reaction should be removed promptly to avoid temperature increases that can lead to runaway reaction, and hot spot formation that would result in catalyst deactivation [18].

$$n\,CO + (2n+1)H_2 \dot{\Rightarrow}\ C_nH_{(2n+2)} + n\,H_2O \qquad \Delta H_{298K} = -165\,\frac{kJ}{mol} \qquad \text{Eq. 9}$$

Commercially, the most active metals for the FTS are iron (Fe), cobalt (Co), ruthenium (Ru) and nickel (Ni) [19]. Under normal operation condition, Ni catalyst favors methane (CH_4) formation; thus, it is rarely used in FTS. On the other hand, Ru catalysts are the most active Fischer-Tropsch catalysts; but it is too expensive with limited reserves that make it unsuitable for industrial scale. These factors leave Fe and Co as the commercial catalyst for FTS.

Fischer-Tropsch reactor commercial designs have focused on temperature control, heat removal and desired product distribution. There are three types of reactors used in the large-scale GTL plants: (1) tubular fixed bed reactor (TFBR), (2) fluidized bed reactor (FBR), and (3) slurry phase bubble reactor (SPBR). Each reactor technology has their

advantages and disadvantages. The tubular fixed bed reactor (TFBR) design has been widely used in the industry for many years, it's mainly consists of multiple tubes in parallel packed with catalyst particles and immersed in water for heat removal. Syngas flows through the top of the catalyst bed that is operated at 10-45 bar and 180-250 ℃. TFBR (gas phase) are easy to operate, don't need catalyst separation device and offer excellent reactant diffusivity. The main disadvantage of TFBR is the non-uniform temperature control in the radial direction of the bed which can lead to local hot spot formation and catalyst deactivation. To overcome the limitation of the gas phase operation another reactor layout has been designed, which known as slurry phase bubble reactors (SPBR) that is mainly composed of a vessel containing slurry (liquid, wax products, and catalyst powder). Syngas bubbled through the liquid phase while contacting with the catalyst. To minimize the methane selectivity the temperature in SPR is always below 250 ℃. Compared to other reactors, the SPBR were designed to solve the temperature control problem as the result of the liquid phase heat capacity. Therefore, they run under isothermal condition because of the high heat capacity of the liquid medium. The major drawbacks of the SPBR are the low conversion, the difficulty in the catalyst separation, and the slow diffusion of the syngas through the liquid; therefore, selecting of particular reactor design is a trade-off process depending on the required product distribution and the process design.

1.5. Supercritical Fluids (SCF) in the FTS

In order to mitigate the weakness of the gas-phase operation, a unique reaction media had been created using supercritical fluids while allowing for fixed bed operation [7-8]. Supercritical fluids are those fluids that present at temperature and pressure higher than their thermodynamic vapor-liquid critical point [22]. SCF is considered as a unique reaction media that offer single phase operation for the FTS, greater diffusivity and lower viscosity than that of liquids, an adequate density that allows for considerable dissolution power and improve the *in-situ* wax removal from the catalyst [23]. The current research aims for studying the catalyst selectivity for fixed bed reactors that operate under supercritical fluids as a non-conventional reaction medium. There are many solvents that can be used as supercritical fluids solvents such as pentane, hexane, heptane or higher alkanes [20]. The first reported utilization of supercritical fluids in FTS was in 1989 by Fujimoto [21] when they compared the performance of TFBR under three different phases: liquid phase (n-hexadecane in trickle bed), gas phase (nitrogen as makeup) and SC phase (n-hexane). They found that in SC reaction the diffusion of the syngas and olefin is much faster compared to the other phases. Also, they suggested a selection criteria for the SC-FTS fluid as follow [23]:

1) The reaction temperature and pressure must be higher than the fluid critical properties.
2) The fluid should be inert under reaction conditions and at the same time does not affect the catalyst activity.

They first reported role of SC reaction media in the facilitation of the wax removal from the catalyst pores. Jacobs *et al*. [24] studied the advantages of running the FTS reaction under SCF, and they reported less condensation of the wax on the catalyst in supercritical media (using C_5/C_6) in comparison with the gas phase media. Moreover, they

observed an increase in the conversion in SCF media as a result of the improvement in the catalyst accessibility after wax removal from the active site, combined with the decrease in carbon dioxide and CH_4 selectivity. Similarly, Huang and Roberts reported [25] increase in the catalyst active site and enhanced in the olefin reabsorption in the SCF media.

Another advantage of the SCF media is the improvement of the reactants and products diffusivity which is the problem for the slurry reactor or in the wax-filled pore space in the gas phase operation. Bukur et al. [26] studied FTS in fixed bed reactor under both conventional gas phase operation (P =1.48 MPa) and nonconventional supercritical operation (propane or n-hexane as supercritical fluids; P =4.1-7.0 MPa), as well as in SPR. They observed that the catalyst activity in SCF media was higher than conventional FBR and SPR. They attributed that to the higher diffusivity of the reactants in the SCF media. Moreover, the SCF media improved the thermal management in the reactor which decreases the possibility of the hot spot formation and runaway reaction. Robert et al. [25] studied the effect of using SCF instead of the gas phase in FTS on the temperature profile along the reactor bed. They found that the maximum temperature deviation along the reactor is 15 ℃ in the gas phase compared to 5 ℃ in the SCF phase.

Based on the literature it can be inferred that SCF media enhance the wax extraction that gives higher accessibility to the active sites, decrease the diffusivity resistance (higher conversion) and better temperature control.

1.6. FTS Mechanism

The kinetic model can be derived empirically, semi-empirically or mechanistically. The most accurate approach is the mechanistic which uses sequential reaction pathways

(i.e., mechanism) to develop the detailed kinetics model. The mechanism of a chemical reaction is a list of elementary chemical reaction to explain the observed rates and product [27]. The FTS mechanism has extensively been studied, but the specific mechanism remains uncertain. However, the FTS reaction is accepted to consider as polymerization reaction in which the reaction between the CO and H_2 takes place on the surface of the active site. In FTS mechanism almost all the reaction elementary steps consist of: (1) adsorption of the reactant on the surface, (2) chain initiation, (3) chain growth/propagation, and (4) chain termination and product desorption from the catalyst surface [28].

There are different mechanisms for FTS based on the different intermediate steps. The main polymerization scheme that have been proposed is: Alkyl mechanism, CO insertion mechanism, enol mechanism, and alkenyl mechanism.

Brady and Pettit [29] proposed the alkyl mechanism (Figure 4) that begins with the dissociation of the CO into C and O. They argued that the chain growth started when the methylene ($CH_2.S$) is inserted into the adsorbed metyl species. After that the chain propagation continues by inserting the methylene into the alkyl species. The termination steps take place by reduction of alkyl chain to give paraffin or hydride elimination to give olefin [30]. The alkyl mechanism gives an advantage for the paraffin formation rather than the olefin formation, thus it underestimates the olefin selectivity [31].

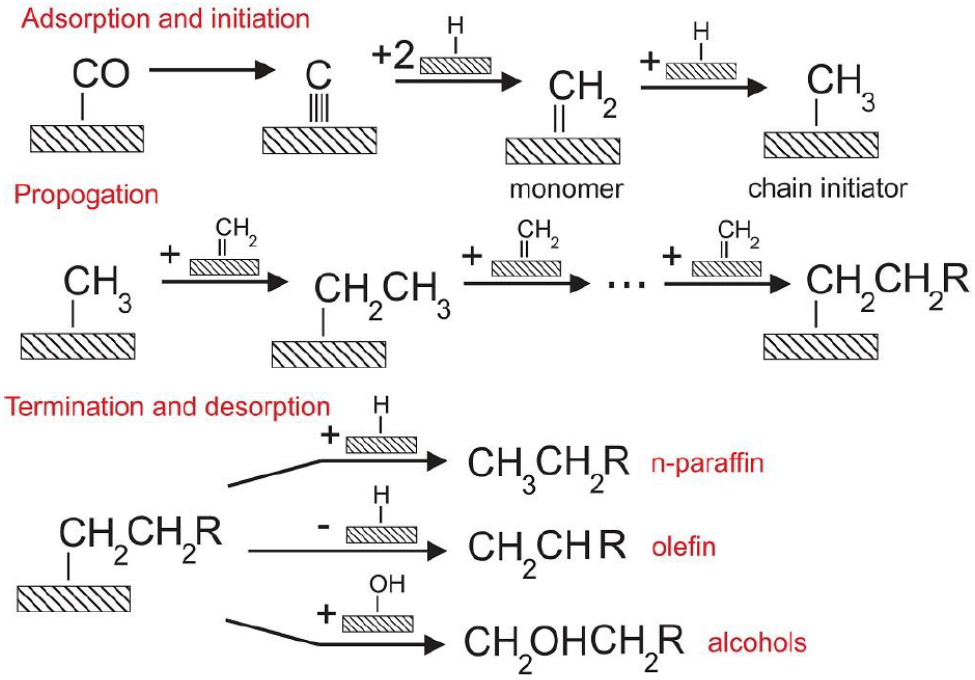

Figure 4: Schematic of the alkyl mechanism. Reprinted from [32]

The second proposed mechanism is the CO insertion mechanism (Figure 5) which is developed by Pichler and Schulz [32]. According to this mechanism, the initiation step starts with the hydrogenation of the adsorbed CO. The propagation step requires the insertion of adsorbed CO into a metal- alkyl bond to form acyl species CH(OH)R., which is then hydrogenated, and oxygen removed to produce the alkyl species similar to the alkyl mechanism. Finally, the termination step happens by the hydrogenation of the alkyl species to give n-paraffin or by β-hydrogen removal to give 1-olefin [33]; also, the CO insertion mechanism confirm the production of the alcohols and the aldehydes .

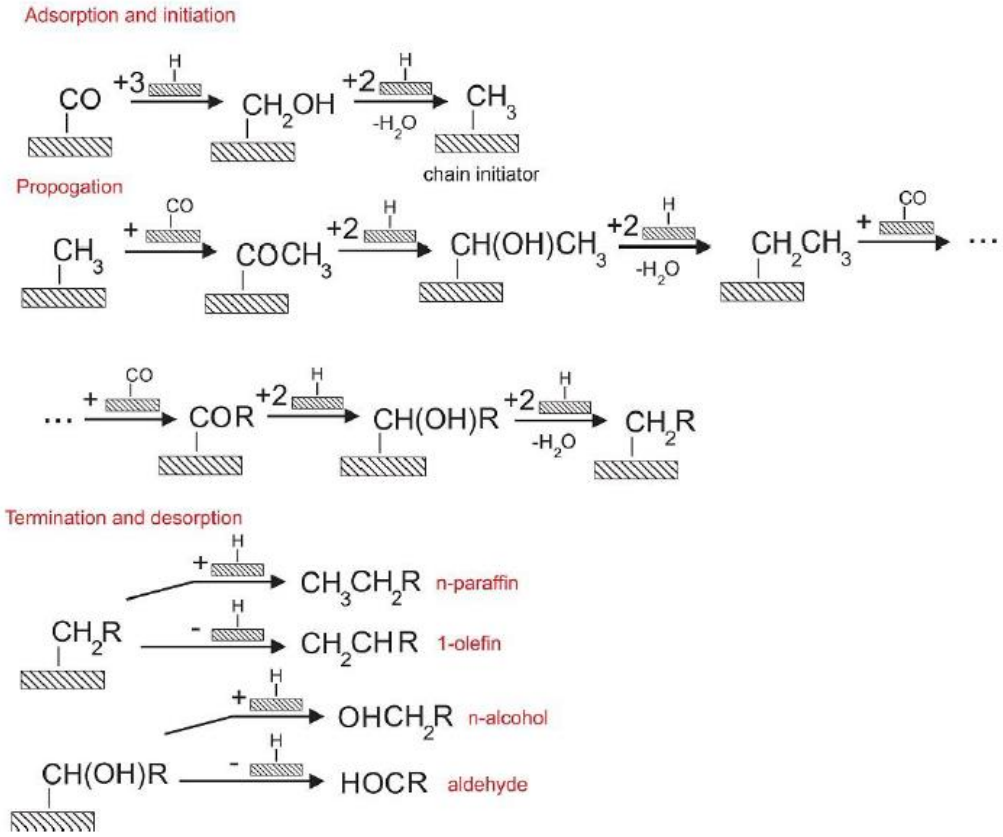

Figure 5: Schematic of the CO insertion mechanism. Reprinted from [32]

The third proposed mechanism for FTS is the enol mechanism. Eidus et al. [27] proposed that the chain initiation start with the hydrogenation of the CO to give us the enol group (hydroxycarbine CHOH). They suggested that the chain growth occurs through the polymerization of the enol groups (M=CHOH). Also, Storch et al. [34] suggested that the chain propagation takes place by the condensation of the enol groups.

1.7. Kinetic Models for SCF-FTS

The quality of a detailed kinetic model is correlated to the SCF-FTS reaction mechanism understanding. The FTS is a polymerization reaction, in which the products distribution can be lumped according to the ideal Anderson-Schulz-Flory (ASF). The model suggests that the growth and the termination steps are independent of the chain length and temperature. As a result, the chain growth probability (α-value) has been defined as follows:

$$\alpha = \frac{N_{n+1}}{N_n} = \frac{R_p}{R_p + R_t} \qquad \text{Eq.10}$$

where R_p and R_t are the rates of propagation and termination, respectively. According to ASF assumptions, a plot of ln ($\frac{W_n}{n}$) vs. n should give a straight line with $\ln(\alpha)$ as slop:

$$ln\left(\frac{W_n}{n}\right) = n\, ln(\alpha) + ln\left[\frac{(1-\alpha)^2}{\alpha}\right] \qquad \text{Eq.11}$$

Several studies reported experimental data in FTS and SCF-FTS that has a deviation from the ideal ASF distribution [4-5]. Elbashir and Roberts [37] observed a significant deviation from the ideal ASF distribution as shown in Figure 6. They suggested representing the product distribution of SCF-FTS by more than one alpha value for the different hydrocarbons range.

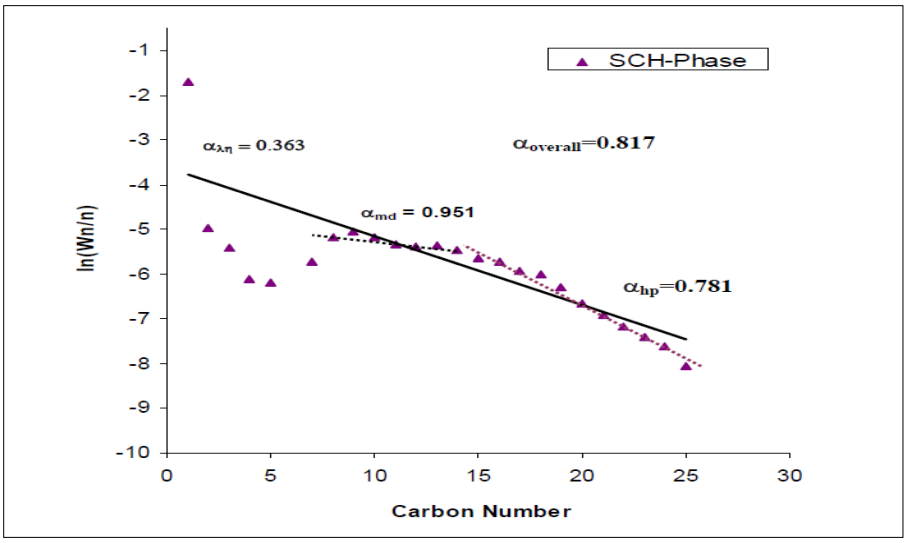

Figure 6: Hydrocarbon product distribution in SC-hexane FTS. Reprinted with permission from [37]

Subramaniam and Fan [38] estimated an effective rate constants (ηks) for SCF-FTS based on the steady state gas conversion. The rate constants were derived assuming pseudo first order in H_2 partial pressure. Elbashir and Roberts [39] developed a partial pressure based kinetic model for SCF-FTS reaction over 15% Co/Al_2O_3 catalyst that used to calculate CO consumption rate and CH_4 formation rate. However, the model reportedly worked better in the gas phase based on their experimental investigations. They also observed that the model over predicted methane selectivity while under predicted CO consumption rate under SCF-FTS conditions compared to their experimental data. They also suggested that the inability of the model to predict the performance of FTS under SCF media could be from using the partial pressure (concentration) of the reactant in the rate equations rather than their activities. To improve this model Mogalicherla and Elbashir [40] account for the non-ideality of the SCF-FTS by using the fugacity parameters to represent the reactant concentrations. However, they did not extend the fugacity-based

kinetic model to predict the full hydrocarbon product distribution–for the non-ideal reaction mixture of SCF-FTS. Todic et al. [41] developed a comprehensive micro-kinetic model for gas phase FTS based on carbide mechanism which predicts the product distribution over Co-Re/Al_2O_3 catalyst up to C_{15}. One of the main focus of this work is to further improve the preliminary model of Elbashir and Roberts [39] of the kinetics of the SCF-FTS regarding its accountability for the hydrocarbon product distribution obtained using Todic et al. [41] methodology that is based on alkyl mechanism first proposed by Brady and Pettit[29].

2. RESEARCH PROBLEM AND OBJECTIVES

One of the key challenge in the Qatar national vision 2030 is to develop a gas industry that can provide Qatar and the world with clean energy sources [42]. Qatar is investing heavily in the development of GTL process in many fronts since the fuels obtained from GTL process are considered ultraclean fuels that are free of sulfur and aromatics. This research work is focused on developing better modeling tools to predict the catalyst behavior in terms of both activity and selectivity for two of the most important stages of the GTL process, the reformer unit and the Fischer Tropsch reactor. In order to achieve this goal, a semi empirical modeling approach was developed and tested for different reaction conditions and catalytic systems.

The first phase of this research work focused on the development of a model that predict the deactivation mechanism of several Ni-based catalytic systems on the DRM reaction. One of the main problems related to the DRM reaction is the catalyst deactivation owing to the multiple sources of the carbon in the process, which lead to accumulation of the carbon on the catalyst surface. The major benefit of the outcome of this research work is that it helped in the catalyst design and in the selection of optimum reaction conditions that sustain the catalyst activity for long TOS. In this part, the GPLE model was used to study the catalyst activity and deactivation of seven catalytic systems and a quantitative assessment of carbon deposition and sintering of these catalysts at specified reaction conditions was conducted.

The second part of this research work is focused on developing a model to predict the FTS hydrocarbon product distribution when conduct the reaction in the non-conventional supercritical fluids (SCF-FTS). This model is important in the process design and commercial scale-up of the SCF-FTS reactor unit. Although the FTS kinetics has extensively been studied, the attempts to capture a full product distribution for supercritical FTS is yet to be developed. Earlier studies focused on predicting the CO conversion and CH_4 selectivity of SCF-FTS [40] but did not account for the full hydrocarbon product distribution. Additionally, there are limited knowledge available in literature that accounts for the deviations from the ideal ASF distribution in the SCF-FTS. Therefore, this study aimed at modelling the products distribution of the SCF-FTS using typical FTS cobalt-based catalyst (15 wt. % Co, 0.5 wt.% Ru on Al_2O_3). This model was verified by running an experimental campaign on FTS in SCF media using hexane as supercritical solvent. The experimental data obtained from this campaign has been utilized to develop a detailed kinetic model based on the hydrocarbon selectivity from (C_1 to C_{15}). The elementary steps for the kinetics model is proposed to follow the alkyl mechanism on the cobalt catalyst [43]. To estimate the kinetic model parameters a genetic algorithm code has been developed in MATLAB, and the model validation conducted using experimental data. Finally, a detailed kinetic model has been proposed for the FTS-SCF, which accounts for the extended ASF deviations in SCF runs.

3. RESEARCH METHODLOGY

The present research work is structured in two major activities:1) modeling of the catalyst deactivation in the DRM reaction 2) modeling of the catalyst selectivity in SCF-FTS reaction. The modeling of catalyst deactivation uses GPLE model to predict the catalyst deactivation mechanism has been described in section 3.1 while the modeling of the catalyst selectivity of the SCF-FTS reaction is described in detail in section 3.2. The former kinetics study is further divided into the following sections: the development of the kinetics model, the experimental campaign, and the genetic algorithm section.

3.1. Modeling of Catalyst Deactivation

Modeling of catalyst deactivation rates using empirical data can shed more light to the underlying principle involved and predict mechanistic pathway of catalyst deactivation. Therefore, modeling of catalyst deactivation rates under empirical conditions that simulates the actual catalyst performance has a considerable impact on the future catalyst design to improve the process.

Accordingly, there is a significant need to interpret the catalyst deactivation phenomena thereby improve the catalyst performance.

3.1.1. Generalized Power Low Expression (GPLE)

Different models have been used in the literature to deal with the catalyst deactivation, starting from the power law equation (PLE), which assumed that the catalyst

activity would go to zero after a long time on stream. The decay equation can be expressed as follows [44]:

$$-\frac{da}{dt} = P(T,C)a^d \quad \text{Eq.12}$$

where a is the normalized activity that can be defined as the reaction rate at any time divided by the initial reaction rate, d is deactivation order, T is temperature, C is concentration and $P(T,C)$ represent the kinetics function. Using of the PLE to model the catalyst deactivation always accompanied with several disadvantages such as: 1) change of the deactivation order will give different kinetic parameters, and 2) the order of the deactivation fitting change with time and temperature. Moreover, the deactivation of the data shows that after a long TOS, the activity will reach a steady state activity (SSA) which is in contrast with the main assumption in the PLE model. This inadequacy proposes that the PLE model is not suitable to represent the observed phenomenon. Nevertheless, an analysis of the deactivation data shows that the fitting can be improved by using higher order of the deactivation, which means increase of the non-linearity of the equation. To mitigate the disadvantages of the PLE, GPLE model has been developed to account for the SSA. The GPLE modeled the catalyst deactivation rate as follow:

$$-\frac{da}{dt} = k_d\, P(c)_d\, a^d + constant \text{ ; or} \quad \text{Eq.13}$$

$$-\frac{da}{dt} = k_d P(c)_d (a - a_{ss})^d \quad \text{Eq.14}$$

where k_d is deactivation rate constant, $P(c)_d$ represent the kinetic function that depends on the concentration and a_{ss} is the SSA. Argyle et al. [45] studied the effect of including the reactant concentration in FT reaction (CO, H_2, and H_2O) on the catalyst deactivation

rate. Argyle et al. [45] found that there are no significant improvements in the fitting results were obtained by including the reactant concentration. Accordingly, they assume that the deactivation rate is independent of the concentration. The solution of the activity equation was obtained by applying the boundary condition that at the initial condition, $a = 1$. The linearized solution for the GPLE equation for the first order deactivation process is:

$$a(t) = (1 - ass)\, exp(-k_1 t) + ass \qquad \text{Eq.15}$$

While for the second deactivation rate:

$$a(t) = (k_2 t + (1 - ass)^{-1})^{-1} + ass \qquad \text{Eq.16}$$

The deactivation rate constant k_d and $\boldsymbol{a_{ss}}$ are estimated using the nonlinear least squares regression in Microsoft Excel.

Argyle et al. [45] divided the overall activity into two subcomponents as shown in Figure 7, they represents the initial deactivation by sintering (a_1) that reaches the steady-state fast and can be fit with second-order GPLE, and 2) the slower and a longer period of deactivation by carbon deposition is represented by (a_2) that can be fit with first order GPLE. They defined the fraction loss of the activity (f_i) as follow:

$$f_i = 1 - a_i \qquad \text{Eq.17}$$

$$f_{tot} = f_1 + f_2 \qquad \text{Eq.18}$$

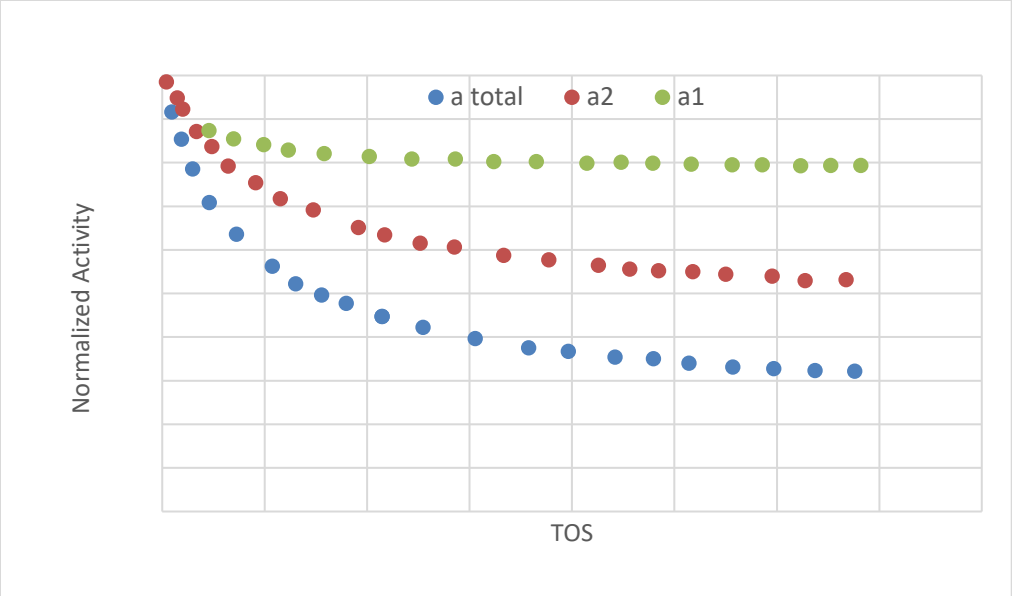

Figure 7: Activity versus TOS data that illustrate the division of the total activity into two different mechanisms. Adapted from [45]**.**

3.1.2. Ni-based Catalysts Selected for the DRM Deactivation Model Development

Seven catalytic systems were selected to study the catalyst deactivation on the DRM reaction, as shown in Table 1. The dry reforming of methane was examined in the bench scale reactor using a vertical quarts reactor at atmospheric pressure. The catalyst bed was prepared by mixing 5.5 mg of catalyst and 100mg of SiO_2 as a diluent. Before the reaction, the catalyst mixture was reduced using H_2 at 650 °C for 1 h. The reaction mixture was mainly consisted of 10% CH_4/10% CO_2/80% He.

The bimetallic (10% Ni_8-Cu_1/Al_2O_3) and monometallic (10% Ni/Al_2O_3) catalyst was prepared using the incipient wetness impregnation method to study the effect of adding Cu promoter in the catalyst performance and catalyst deactivation by coke deposition [46]. The commercial catalyst (20% Ni/Al_2O_3) was tested to examine the effect of changing the reaction temperature in the catalyst deactivation mechanism. The ALD

catalyst was prepared by covering the commercial catalyst with different layers of amorphous alumina overcoat (ALD-1, ALD-5, and ALD-20) used to suppress the catalyst deactivation by sintering [47].

Table 1: Catalytic systems used in the catalyst deactivation study

Catalyst	Test length (hr)	T (^oC)	P (bar)	CH_4/CO_2	X_{CH4o} (%)
10% Ni/Al_2O_3	70	650	1	1	0.47
10% Ni_8-Cu_1/Al_2O_3	70	650	1	1	0.76
Riogen[1] 1	40	650	1	1	0.52
Riogen 2	40	550	1	1	0.31
ALD[2]-1	40	650	1	1	0.50
ALD-5	40	550	1	1	0.18
ALD-20	600	650	1	1	0.45

3.1.3. Methodology of Mechanism Separation

The adopted method to separate the deactivation mechanism can be expressed as follow:

1. The rate versus TOS data were obtained for all the catalytic systems.
2. The rate was normalized by dividing the rate by the initial rate to get the activity.
3. The normalized activity data was fitted to the first and second order GPLE equation.
4. The experimental activity data were analyzed to check if the data can be divided into two deactivation regimes

[1] The industrial catalyst that used in methane reforming
[2] A novel catalyst that produces by covering the alumina catalyst support with pores Al_2O_3 thin film through the atomic layer deposition (ALD)

5. Since the rapid deactivation by sintering reaches the steady state activity after a short TOS t_r. The total loss of the activity ($f_{tot} = 1 - a_{tot}$) for $t>t_r$ was fitted versus TOS for $f_{tot} = f_{1ss} + f_2$. where f_{1ss} is the steady-state loss of the activity from sintering, f_2 is the loss of activity from carbon deposition that can be expressed using first order GPLE.

   $f_{tot} = f_{1ss} + 1 - ((1 - a_{2ss}) \exp(-k_2 t) + a_{2ss})$ for $t>t_r$ Eq.19

   The fitting results will give us the value of f_{1ss} , a_{2ss} and k_2.

6. The calculated constant in step 5 (a_{2ss} and k_2) was used to calculate the activity loss from the carbon deposition (f_2) for all the TOS data:

   $a_2(t) = (1 - a_{2ss})\, exp(-k_2 t) + a_{2ss}$ Eq.20

   $f_2 = 1 - a_2$ Eq.21

7. The total activity loss (f_{tot}) was calculated from the total normalized activity data (a_{tot}):

   $f_{tot} = 1 - a_{tot}$ Eq.22

8. The activity loss from the sintering (f_1) and the activity data of the sintering (a_2) was calculated as follow:

   $f_1 = f_{tot} - f_2$ Eq.23

   $a_1 = 1 - f_1$ Eq.24

9. The activity data of the sintering (a_1) was fitted to second order GPLE to calculate the model parameters (a_{1ss} and k_1).
10. The results were checked by comparing the value of the f_{1ss} that calculated in step 5 with the a_{1ss} ($f_{1ss} = 1 - a_{1ss}$) calculated in step 9.
11. Finally, The Percent of activity loss was calculated using the SSA values.

3.2. Modelling of Catalyst Selectivity

To study the kinetic model for SCF-FTS, our research group designed a strategy, as shown in Figure 8. In the first part, a detailed kinetic model for SCF-FTS was developed based on the alkyl mechanism, and the result was compared with different kinetics models from different mechanism. The purpose of developing a FTS kinetic model was to capture the product distribution up to C15 including the normal parafins and 1-olefins which is not available in literature for SCF-FTS. Subsequently, in the second part of this work, a detailed experimental campaign was conducted to generate the data required to calculate the model parameters. In the third part of the study, the model parameters were generated using genetic algorithm code in MATLAB. Finally, the model results were validated using the mean absolute relative residual (MARR).

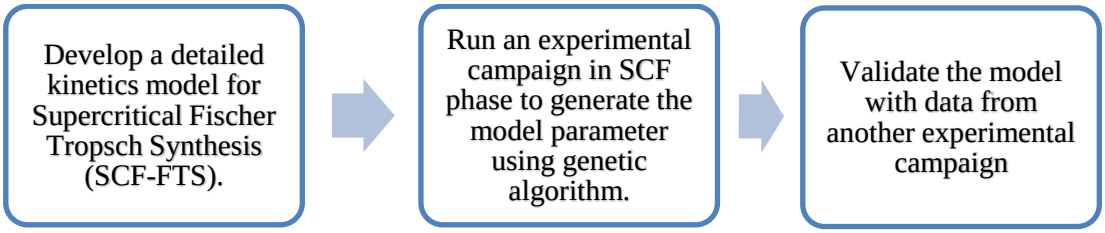

Figure 8: The proposed methodology for the research

3.2.1. Development of a Detailed Kinetics Model

For model simplification, the following assumptions are made:

1. Only one active site is present in the Co catalyst surface.
2. Since we are working in the critical and near critical phase, the resistance of the mass and heat transfer were neglected.

3. The rate determines steps are the termination, propagation, and methyl formation steps.
4. The formation rate of C_n hydrocarbon is equal to the summation of the formation rate of the paraffin and the olefin for that hydrocarbon.
5. The water gas shift (WGS) reaction was neglected, due to negligible selectivity of cobalt catalyst for WGS reaction.
6. The intermediates ($\mathrm{CH_2.S, CH.S,}$ and $\mathrm{C_nH_{2n+1}.S}$) and water do not occupy a significant part of the active site.
7. The rate constant of the 1-olefins desorption is exponentially dependent on the carbon number.
8. The catalyst deactivation has been neglected for simplicity of calculation.
9. The methane formation rate has a different rate constant from the rest of the paraffin.
10. The ethylene formation rate has a different rate constant from the rest of the olefin.
11. The intermediate activity coefficients assume to be unity.

Chemical reactivity in supercritical media

The transition state theory explains the reaction rate between the reactants and transition state complex, assuming a special type of chemical equilibrium. The theory state that the reaction between the reactants occurs through the formation of an intermediate that will proceed to form the final products [48].

$$A + B \leftrightarrow M^* \rightarrow P \qquad \text{Eq.25}$$

The rate equation can be expressed as:

$$Rate = k_{\circ}(\frac{\gamma_A \gamma_B}{\gamma_M^*})[A][B] \quad \text{Eq.26}$$

where $k_{\circ}$ is the rate constant in the ideal system, and $\gamma's$ are the activity coefficient in the mixture.

The equilibrium constant can be expressed as:

$$K^* = \frac{[M^*]\gamma_M^*}{[A][B]\gamma_A\gamma_B} \quad \text{Eq.27}$$

Reaction mechanism

The reaction mechanism for the proposed kinetic model developed using Langmuir-Hinshelwood (LH) kinetics. First, the reaction will begin with the adsorption of the reactant in the surface, which happened in three steps: (1) the dissociative adsorption of the hydrogen on the surface with K_1 as equilibrium constant, (2) the molecular adsorption of the carbon monoxide on the active site with K_2 as equilibrium constant, followed by (3) the dissociative adsorption of the CO intermediate with K_3 as equilibrium constant. Secondly, the initiation of the building block to produce the methyl ($CH_3.S$). van Barneveld and Ponec [49] reported that the formation of ($CH_3.S$) intermediate is an irreversible process. So, the formation of ($CH_3.S$) will have k_6 as Arrhenius constant, and the monomer ($CH_2.S$) will have K_5 as equilibrium constant. Thirdly, the propagation of the chain to produce higher hydrocarbons with k_{pro} as Arrhenius constant. Finally, the termination of the intermediate to produce the products represented by four termination constants: (1) formation of the methane has (k_{par1}) as constant, (2) termination of the ethylene has $\left(k_{olef2}\right)$ as constant, (3) producing of the rest of the paraffin has (k_{par})as

constant, (4) producing of the rest of the olefin has (k_{olef}) as constant. The reaction pathway for the alkyl mechanism is shown below:

Surface Adsorption:

$$H_2 + 2S \overset{K_1}{\Leftrightarrow} 2H.S \quad \text{Eq.28}$$

$$CO + S \overset{K_2}{\Leftrightarrow} CO.S \quad \text{Eq.29}$$

$$CO.S + S \overset{K_3}{\Leftrightarrow} O.S + C.S \quad \text{Eq.30}$$

Initiation of the building block:

$$C.S + H.S \overset{K_4}{\Leftrightarrow} CH.S + S \quad \text{Eq.31}$$

$$CH.S + H.S \overset{K_5}{\Leftrightarrow} CH_2.S + S \quad \text{Eq.32}$$

$$CH_2.S + H.S \overset{k6}{\rightarrow} CH_3.S + S \quad \text{Eq.33}$$

Propagation:

$$C_nH_{2n+1}.S + CH_2.S \overset{k_{pro}}{-} C_{n+1}H_{2n+3}.S + S \qquad (RDS) \quad \text{Eq.34}$$

Termination:

$$C_nH_{2n+1}.S + H.S \overset{k_{par}}{-} C_nH_{2n+2} + 2S \qquad (RDS) \quad \text{Eq.35}$$

$$C_nH_{2n+1}.S \overset{k_{olef}}{-} C_nH_{2n} + H.S \qquad (RDS) \quad \text{Eq.36}$$

$$H.S + CH_3.S \overset{k_{par1}}{-} CH_4 + 2S \qquad (RDS) \quad \text{Eq.37}$$

$$C_2H_5.S \overset{k_{olef2}}{-} C_2H_4 + H.S \qquad (RDS) \quad \text{Eq.38}$$

where K_i refers to the thermodynamic equilibrium constant and k_i to the Arrhenius constant.

$$K_i(T) = A_i \, exp\left(\frac{-\Delta H_i}{RT}\right) \quad \text{Eq.39}$$

$$k_i(T) = A_i \, exp\left(\frac{-E_i}{RT}\right) \quad \text{Eq.40}$$

Determination of the reaction rate expression

The determination of the rate equations has been conducted using the Langmuir-Hinshelwood-Hougen-Waston (LHHW) approach following the alkyl mechanism. Example of the calculation of methane rate are shown below while the rest of the calculations was listed in Appendix A.

From Eq.37 the rate of formation of methane is expressed as follow:

$$R_{CH_4} = k_{par1}[CH_3.S][H.S] \quad \text{Eq.41}$$

The methane formation rate was calculated by assuming quasi-steady state for ($CH_3.S$) which is produced in Eq.33 and consumed in Eq.34 and Eq.37.

$$\frac{dCH_3.S}{dt} = k_6[CH_2.S][H.S] - k_{par1}[CH_3.S][H.S] - k_{pro}[CH_3.S][CH_2.S] \quad \text{Eq.42}$$

At steady state $\frac{dCH_3.S}{dt} = 0$ Eq.43

The chain growth probability for a molecule having n number of carbon atoms α_n is defined as follows:

$$\alpha_n = \frac{[C_nH_{2n+1}.S]}{[C_{n-1}H_{2n-1}.S]} \quad \text{Eq.44}$$

$$\alpha_1 = \frac{[CH_3.S]}{[H.S]} \quad \text{Eq.45}$$

Then, α_1 has been calculated accordingly from rearrangement of Eq.42 and Eq.43.

$$k_6[CH_2.S][H.S] = k_{par1}[CH_3.S][H.S] + k_{pro}[CH_3.S][CH_2.S] \quad \text{Eq.46}$$

$$\alpha_1 = \frac{k_6[CH_2.S]}{k_{par1}[H.S]+k_{pro}[CH_2.S]} \quad \text{Eq.47}$$

The rate equation of the methane was re-written by the substitute of α1 from Eq. 47 as follow:

$$R_{CH_4} = k_{par1}\,\alpha_1[H.S]^2 \quad \text{Eq.48}$$

After writing all the intermediate rate equations at each mechanistic step for all the n-paraffin and 1-oleffen from C1-C15 and working up the algebra. The final rate equations as a function of the intermediate concentrations was determined as follows:

$$R_{C_1} = k_{par_1}\,\alpha_1[H.S]^2 \quad \text{Eq.49}$$

$$R_{C_2} = k_{par}\,\alpha_2\alpha_1[H.S]^2 + k_{olef_2}\,\alpha_2\,\alpha_1[H.S] \quad \text{Eq.50}$$

$$R_{C_n} = \prod_{i=1}^{n}\alpha_i\left[k_{par}[H.S]^2 + k_{olef}[H.S]\right] \qquad n > 1 \quad \text{Eq.51}$$

The intermediate concentrations were obtained from the back substitution of the rate constant value as follow:

$$[H.S] = \sqrt{K_1 P_{H_2}\gamma_{H_2}}CV \quad \text{Eq.52}$$

$$[CH_2.S] = K_5\,K_4\sqrt{K_3\,K_2\,\gamma_{CO}\,P_{CO}}K_1 P_{H_2}\gamma_{H_2}CV \quad \text{Eq.53}$$

Regular solution theory for gas-liquid solutions

The aim of the regular solution theory is to predict the activity coefficient in the near supercritical media using the pure component properties of the mixture [50]. This theory provides a method for estimating the non-ideality of the mixture in the non-polar liquid solution. The regular solution theory assumes that the entropy of mixture at constant volume is equal to the entropy at the ideal solution. Also, it assumes that the energy of

interaction between two different molecules equal to the geometric mean of the interaction energies between similar molecules [51]. From these assumptions, they defined the activity coefficient of component J in multicomponent solution as follow:

$$RT\ ln\ \gamma_j = v_j\left(\delta_j - \bar{\delta}\right)^2 \quad \text{Eq.54}$$

$$\bar{\delta} = \sum_i^m \phi_i \delta_i \quad \text{Eq.55}$$

$$\phi_j = \frac{x_j v_j}{\sum_i^m x_i v_i} \quad \text{Eq.56}$$

where δ is the solubility parameter, γ_j is the activity coefficient for component i on the solution, ϕ is the volume fraction, and v is the molar volume.

3.2.2. Experimental Studies

In order to study the effect of each operating parameter in the kinetic model of FTS, a large set of experimental data was required. Seven experimental runs were conducted (Table 2) corresponding to three temperatures levels of experimental data (230 ℃, 240 ℃ and 550 ℃), three total pressures (45 bar, 65 bar, and 80 bar) to capture the critical and the near critical conditions with H_2:CO=2:1 and gas hourly space velocity (GHSV) of 500 (1/h).

Table 2: Experimental conditions conducted for kinetic study

Run No.	Temperature (°C)	Total Pressure (bar)	H_2/CO Ratio	P_{co} (bar)	P_{H2} (bar)
1	230	45	2	6.6	13.3
2	230	65	2	6.6	13.3
3	240	80	2	6.6	13.3
4	240	65	2	6.6	13.3
5	240	45	2	6.6	13.3
6	250	45	2	6.6	13.3

The experimental campaign reported in this work was performed in the bench-scale FTS reactor designed at Texas A&M at Qatar. The bench-scale reactor unit consists mainly of four sections: the first section is the feed delivery system for both liquid (e.g., solvent hexane) and gas (e.g., Syngas, H_2, CO, Ar, and He) streams. The second section is the reactor system, which is a fixed bed 12-inch-long 1-inch diameter reactor tube (SS316). The third section is the product separation setup, which includes the hot trap to separate the wax and the cold trap to separate the permanent gases from the condensates and water. The fourth section is the product analysis system using the on-line gas chromatograph system (GC). The individual section was described in detail in the subsequent sections. The reactor was designed to work under both conventional gas phase and non-conventional SC phase over heterogeneous catalysts such as Co or Fe. The reactor unit has been designed for unattended operation while sustaining safety and system stability, to do that various safety features like interlocks in control system, pressure relief valves and automatic shutdown connected to gas sensors had been designed.

Feed delivery section

The feed delivery section (Figure 9) consists of the feed purification system, flow controller system for liquids and gases flow to the FT reactor, pressure regulators to control the pressure in the system, high-pressure liquid pump HPLC (P-100) and vaporization vessel (V-110).

A typical feed gas lines start at the gas cylinder. Each of the feed gases (syngas, H_2, CO, Ar, and He) pass through the cylinder's pressure regulator and flow restriction and then enter the feed purification section (FP-101,102,103,104) for removal of moisture, COS, transition metal carbonyls, and oxygen. In the top of the purification column, there is a purge line to clean the lines during the initial unit start-up. After purification, the gases pass through a filter, an emergency shutdown valve (ESDV), forward pressure regulator (PV) and mass flow controller (MFC). After passing the mass flow controllers (MFCs) which calibrated specifically for each gas, all the reactants are combining at mixing point through a non-return valve (NRV)

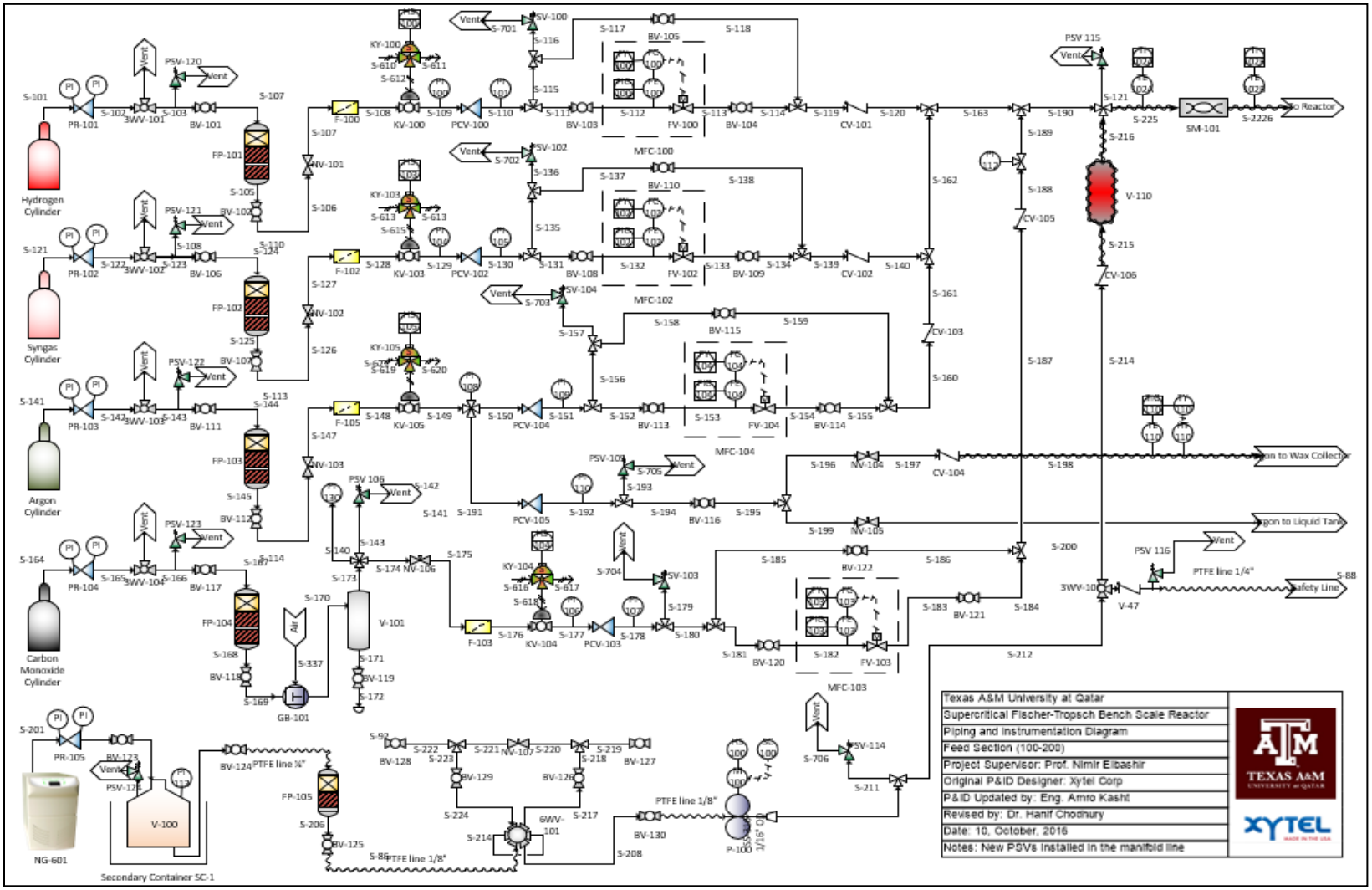

Figure 9: P&ID for feed delivery system

The hexane delivery system consists of solvent storage (V-100), purification column (FP-105), high-pressure HPLC pump (P-100) and vaporization vessel (V-110). A stainless-steel container serves as the solvent tank. The hexane from the tank flows through the purification column into the HPLC pump that transfers the hexane into the vaporizer column. In the vaporizer vessel, the liquid hexane transfer to vapor hexane through the heat provided from the heating tap around the vessel ((HT-113, HTS Amptek, AWO-052-080). Subsequently, the vaporized hexane was mixed with the feed gases in the static mixer (SM-101) located upstream of the FTS reactor to ensure uniform gas mixture (solvent/syngas) before feeding to the reactor.

The MFCs for each gas were calibrated based on the pulse counter in the wet test flow meter (FQI-800, Ritter, TGI-1.4571-PP). As an example, in the calibration of the syngas MFC, we flow different syngas flow rates (25, 50, 125, 150, 200, 300 and 400), and then we monitor the number of the pulses in the Ritter installed in the vent of the cold trap for 30 seconds. Knowing that each pulse accounts for 5 ml/min, we can calculate the actual flow rate at the room temperature. The calibration charts (Figure 10-13) for the flow meters are shown below:

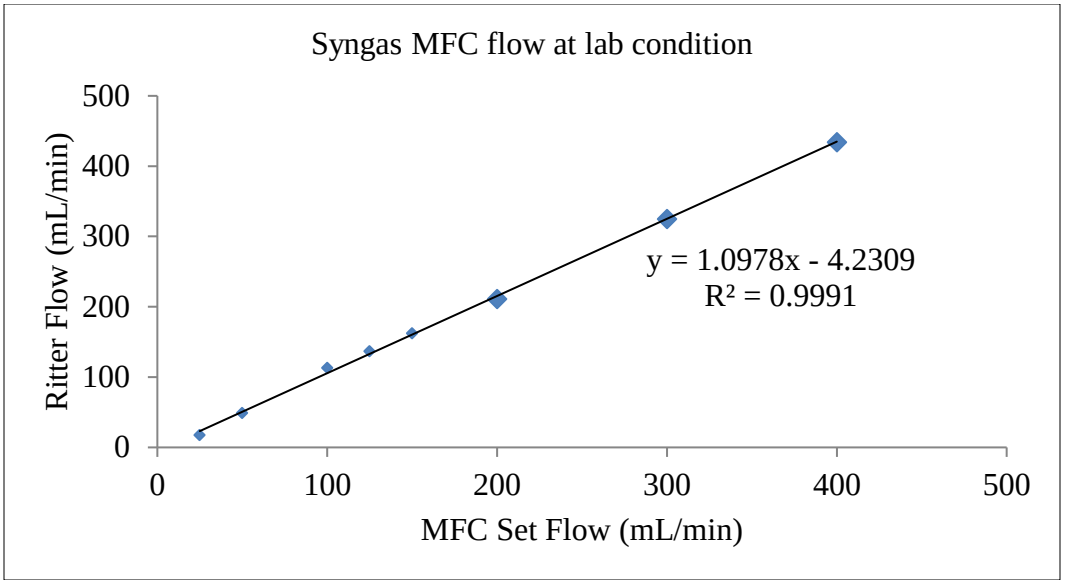

Figure 10: Calibration charts for syngas MFC

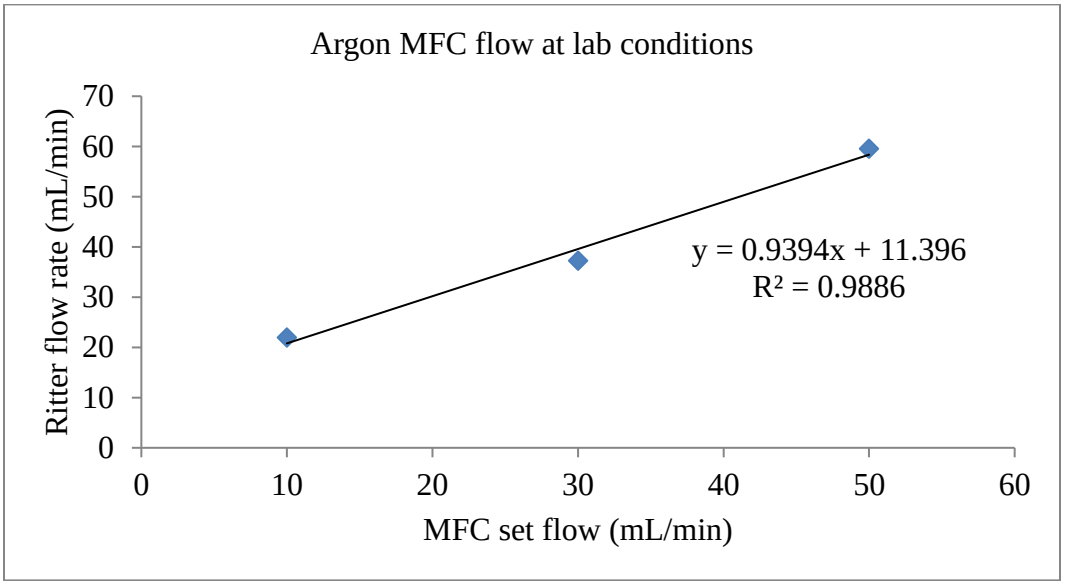

Figure 11: Calibration charts for Argon MFC

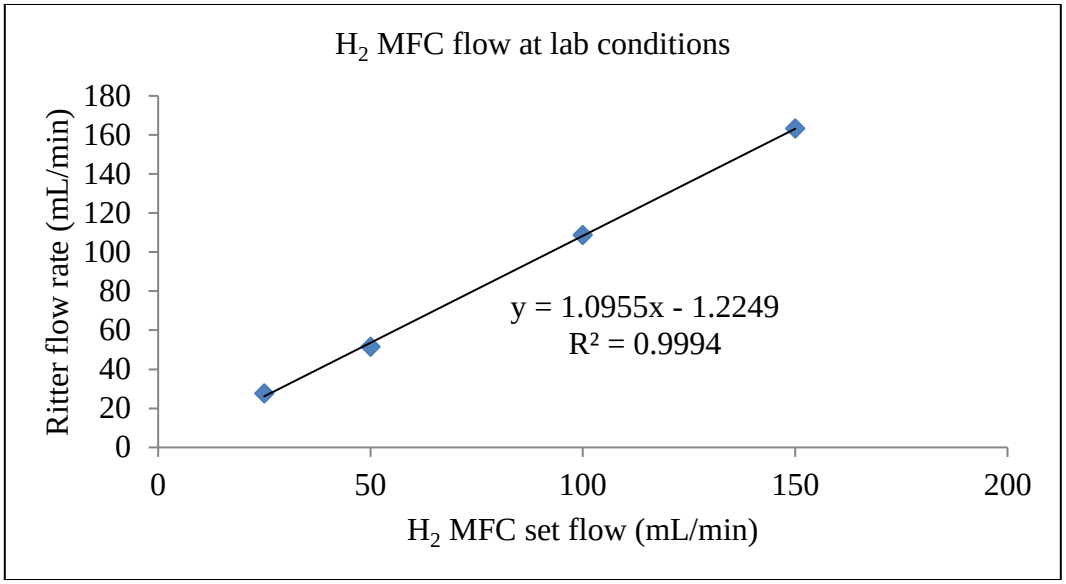

Figure 12: Calibration charts for H_2 MFC

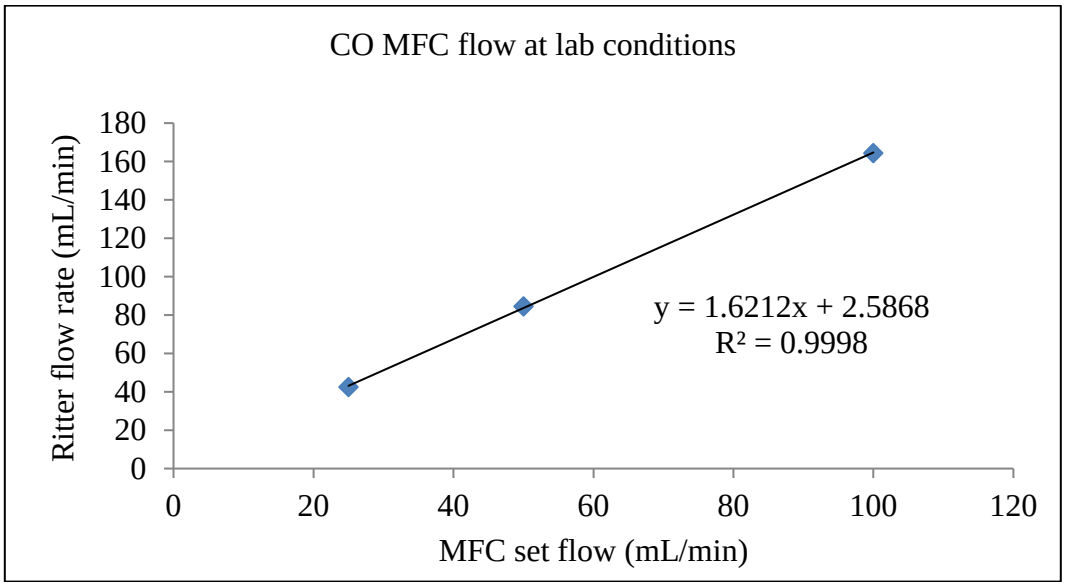

Figure 13: Calibration charts for CO MFC

Reactor setup

The mixed gases mixture enters the customized tubular fixed bed reactor (R-100, Autoclave Engineers, 16” overall length, 12” heated length, 2/3” internal diameter, 1.0” outer diameter, 70 cm^3 net volume in heated zone) at a controlled inlet temperature, mass flow, H_2 /CO ratio, syngas to solvent ratio and inlet pressure. The catalyst used in this campaign prepared and supplied by Auburn University (15 wt.% Co, 0.5 wt.% Ru on Al_2O_3). For the bed preparation, 0.5 g of the catalyst was mixed with 10 g of quartz sand and then loaded in the reactor bed. The reactor tube is vertically installed inside a hollow electric furnace (FRN-100, Applied Test Systems, Lab Furnace 3210) to minimize the axial temperature gradients and control the reactor temperature. The internal reactor temperature is monitored and controlled using three thermocouples (TE-103,104,109, Omega, KMQXL-020G-12) embedded axially inside the catalyst bed. The reactor pressure is controlled by the backpressure regulator (BPR) (PV-115, Badger Meter,1001GCN36SVOSP01ST), which was located between the reactor and the hot trap. The BPR can build up pressure in the reactor up to 150 bar by restricting the outflow from the reactor.

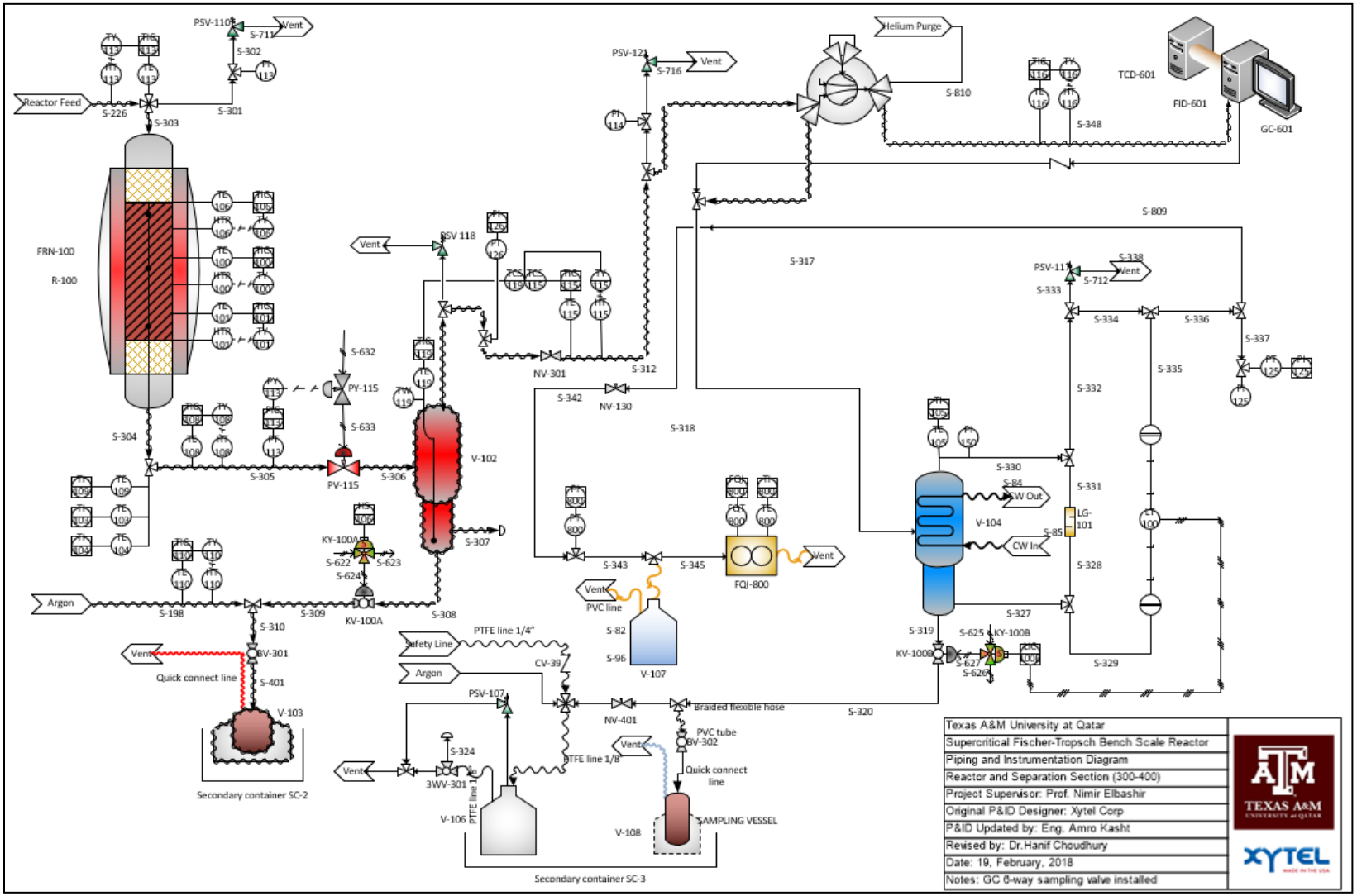

Figure 14: P&ID for the reaction and separation system

Product separation

In order to separate, the product of the FTS the outlet stream from the reactor passed through two flash separation, as shown in Figure 14. The first one is the hot trap (V-102, Xytel, 1053-V102,2.0 L) surrounded by a heating tap and insulated by glass wool and aluminum foil. The hot trap is set at 150 ℃ to settle down the entire heavy hydrocarbon in the wax collector for further analysis. The line connecting, the reactor with the hot trap and the on-line GC and the wax collection vessel are heated to 150 ℃ to avoid any wax condensation. The gases products leave the hot trap from the top towards the on-line GC system through a 6-way selecting valve (6WVS-101, VICI Valco, 300 °C, 150 Bar pressure) where a fraction of the gas was sampled to the GC. The remaining gases were directed towards the cold trap, which is cooled using cold coils with chilled water at 4 ℃. The liquid products condense by the cold trap are collected in a 20L polyethylene tank, and liquid samples are collected periodically in a sampling vessel for off-line GC analysis. The permanent gases leave from the top of the cold trap and pass throw Ritter flow before vented through the ventilation system.

Product analysis system

The products from our experiment consisted of three phases: gas, liquid (from the cold trap) and wax (from the hot trap). The gas phase products are analyzed using dual on-line GC (GC-601, Shimadzu, GC-2014) with both thermal conductivity detector (TCD-601, Shimadzu, TCD-2014) and flame ionization detector (FID-601, Shimadzu, FID-2014)). The gas coming from the top of the hot trap was injected in the GC through a 6-way sampling (6WVS-101, VICI Valco, 300 °C, 150 Bar pressure) installed in a hotbox.

The hotbox temperature is always maintained at 150 °C using a temperature controller to avoid condensation of wax in the 6-way valve. The lines between the hot trap and the GC are kept at 150 ℃ to avoid any condensation of the wax in the analysis system.

There are three detectors on the on-line GC, TCD-1, TCD-2, and FID. TCD-1 detects the presence of the permanent gasses (N_2, Ar, CO, CO_2, CH_4, C_2, O_2, and H_2S). From TCD-1 peaks area, CO conversion and methane selectivity were calculated. Since argon does not participate in the FTS reaction, it is used as an internal standard to calculate the outlet flow of CO by using a pre-calculated response factor (Figure 15). The response factor was calculated by flowing syngas at different flow rates (10-200) NmL/min while keeping the argon flow constant, thus producing a graph of the peak area ratio (PA_{CO}/PA_{AR}) against the CO flow rate as shown below. The trend line equation was used to calculate the carbon monoxide outflow as follows:

$$Q_{CO,out} = \left[\frac{\left(\frac{PA_{CO}}{PA_{AR}}\right)+b}{a}\right] \quad \text{Eq.57}$$

$$CO\ consumption\ \left(\frac{nml}{min}\right) = \left[\frac{Q_{syngas,in}}{3} + Q_{CO,in}\right] - Q_{CO,out} \quad \text{Eq.58}$$

where $Q_{CO,out}$ is the outlet flow rate of the CO, “a” is the slop and “b” is the intercept.

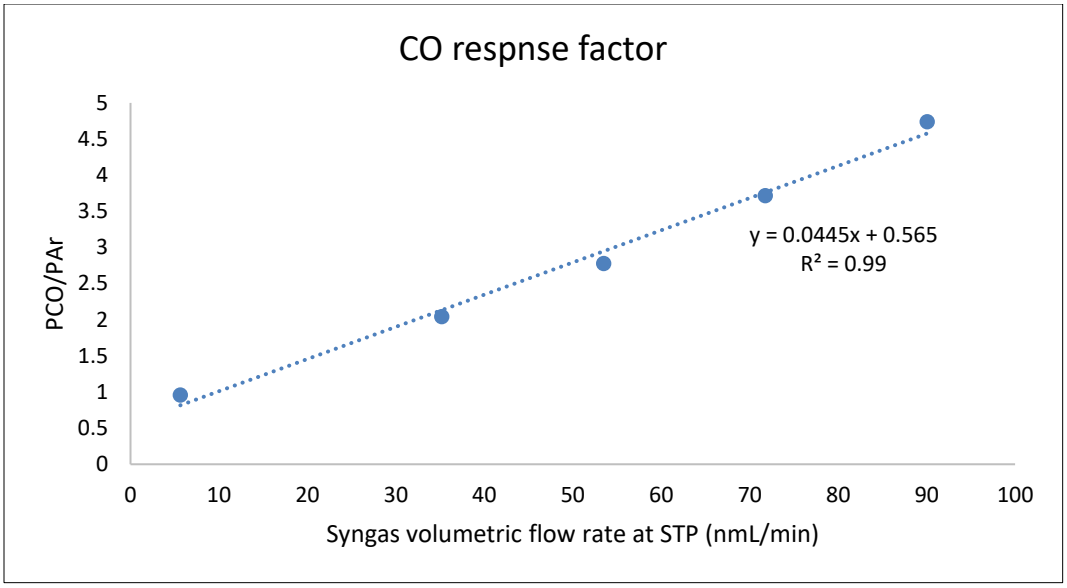

Figure 15: CO response factor

The methane formation rate and selectivity are calculated using a calibration gas with (10.09 mol% CO and 4.0 mol % CH_4 (n_{CH4}/n_{CO} molar ratio =0.397)) to find the response peak area (PA_{CH4}/PA_{CO}) and relate the CO flow rate to CH_4 flow rate as below:

$$Q_{CH4,out} = \left(\frac{PA_{CH4,out}}{PA_{CO,out}}\right) . \left[\frac{\frac{n_{CH4}}{n_{CO}}}{\frac{PA_{CH4}}{PA_{CO}}}\right] . \; Q_{CO,out} \qquad \text{Eq.59}$$

where $PA_{CH4,out}$ and $PA_{CO,out}$ are the peaks area of CH_4 and CO calculated from TCD-1.

The FID detector analyses the hydrocarbons from C1-C9. Since the TCD-1 and FID detect the same amount of the sample, the methane peak in the FID will be equivalent to the same flow rate calculated from TCD-1. The ratio of the CH_4 formation rate from the TCD-1 over the CH_4 peak area from the FID was used as a reference ratio to calculate the formation rate of (C2-C9) hydrocarbons. On the other hand, the second TCD is used to detect the H_2.

Since the rest of the hydrocarbons (more than C10) were not detected on the on-line FID, the off-line analysis of the liquid samples from the cold trap was performed in a GC-FID. A similar approach is used to calculate the formation rate of hydrocarbons more than C9. However, the CH_4 formation rate was replaced by n-C_8 formation rate ($g/g_{cat}.h$).

3.2.3. Genetic Algorithm

Genetic algorithms (GAs) are an optimization approach based on the principles of biological evolution to find the minimum or the maximum of a function [52]. The concept is based on using objective function (fitness function) to distinguish between a good solution and a bad solution [53]. GAs work with a population consisting of different individuals, and each represents a possible solution to the problem. A fitness score will be assigned according to how good a solution is. The individuals with high fitness score are allowed to reproduce among each other; while the least fit members are less likely to reproduce and so die out [54].

The software environments (e.g., MATLAB) helped in solving difficult problems in many different fields. MATLAB has a dedicated toolbox for the genetic algorithm which provides an easy user interface for the optimization. In our research we build up a MATLAB function to have a statistical error function as well as to help in the plotting of the result.

The code is built with the following inputs:

- Experimental data (temperature, component partial pressure, n-paraffin formation rate, and 1-oleffen formation rate).

- Upper and lower limit for the parameters.
- All the calculated equations to estimate the rate.
- The statistical error formula.
- The minimum acceptable error (f_{val}).

The mean absolute relative residual (MARR) was used as statistical error function to check the model efficiency.

$$\mathrm{MARR} = \sum_{i=1}^{N_{resp}} \sum_{j=1}^{N_{exp}} \left| \frac{R_{i,j}{}^{exp} - R_{i,j}{}^{cal}}{R_{i,j}{}^{exp}} \right| \times \frac{1}{N_{resp} N_{exp}} \times 100\% \qquad \text{Eq.60}$$

where N_{exp} is the number of experimental runs, N_{resp} number of responses, $R_{i,j}{}^{exp}$ is the experimental rate and $R_{i,j}{}^{cal}$ is the calculated rate.

4. RESULTS AND DISCUSSION

4.1. Modelling of Catalyst Deactivation

This section discusses the deactivation study results for seven catalytic systems used in the DRM reaction (Table 3 and Table 4). The study provides a comparison between the catalyst deactivation profile of the following Ni-based catalytic systems: 1) bimetallic and monometallic systems, 2) two commercial Ni catalyst (Riogen) each sample tested at different temperatures, and 3) 20% Ni/Al_2O_3 catalyst prepared in-house and covered with thin layers of pores alumina sheets (ALD1, ALD5, and ALD20). The experimental data fitted to the first and second order GPLE model. The perfectly fitted data went through more analyses to study the deactivation mechanism.

4.1.1. Bimetallic and Monometallic Results

In this part, the mono-metallic ($Ni/\gamma\text{-}Al_2O_3$) and bi-metallic ($Ni\text{-}Cu/\ \gamma\text{-}Al_2O_3$) catalyst performance for 70 h TOS data are compared.

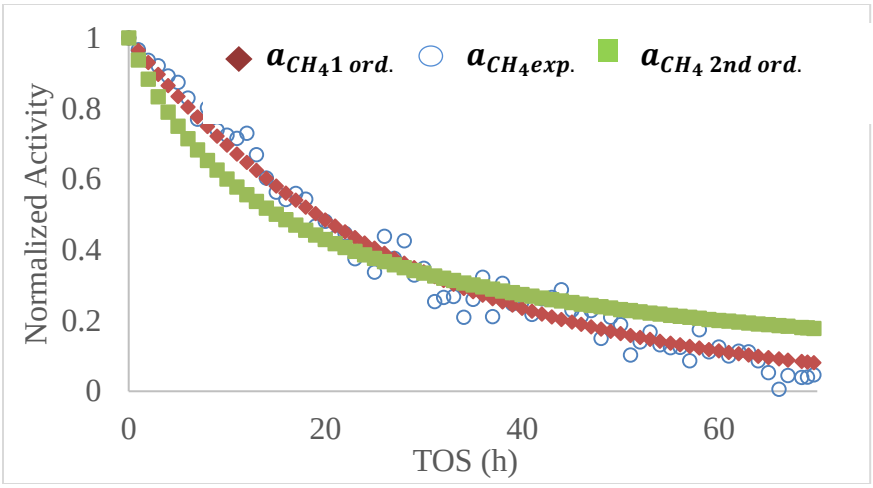

Figure 16: Normalized activity versus TOS for Ni/γ-Al_2O_3 catalyst in DRM reaction at 650 °C, 1 bar, CH_4/CO_2=1, where $a_{CH_4exp.}$ is the experimental methane activity, a_{CH_4}1 ord. is the first order GPLE fitting of methane activity and a_{CH_4} 2nd ord. is the second order GPLE fitting of methane activity

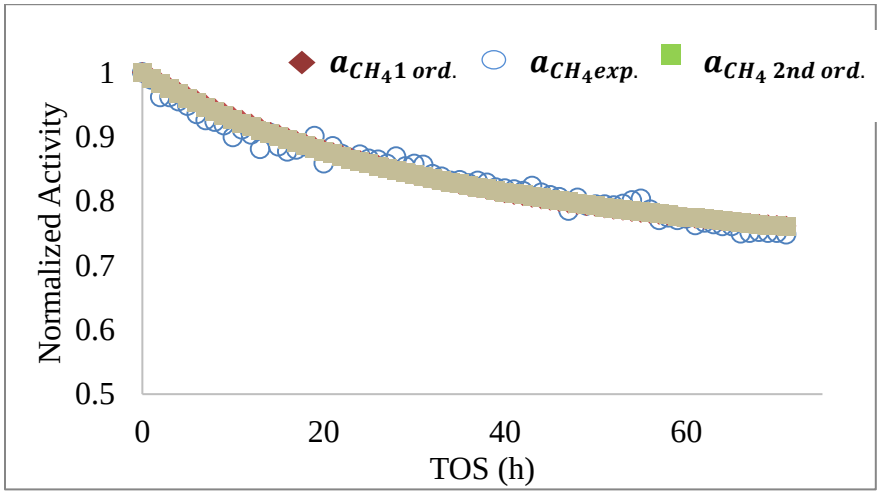

Figure 17: Activity versus TOS for (Ni-Cu/ γ-Al_2O_3) catalyst in DRM reaction at 650 °C, 1 bar, CH_4/CO_2=1

For the mono-metallic Ni/Al_2O_3 catalyst, both the first and second order GPLEs fit the experimental deactivation data quite well with R^2 values of 0.98 and 0.96, respectively (Figure 16). As depicted in Figure 16, the calculated catalyst steady state activity, a_{ss} approaches almost zero given an infinite amount of TOS for both first and

second order GPLE models. This goes against the primary requirement in GPLE fitting that the deactivation must be asymptotic in nature and not reach zero value. In this specific scenario, a_{ss} tends to zero most probably due to the high rate of the carbon deposition, which eventually covers the catalyst surface, preventing accessibility of the reactants to the active site. For the "medium" Cu bimetallic Ni_8Cu_1/Al_2O_3 catalyst (Figure 17), the a_{ss} value calculated using the second order GPLE model for a similar TOS of 70 h was found to be at a much higher 0.62. The a_{ss} value predicted by the second order GPLE model is considerably lower than the a_{ss} value of 0.73 calculated by the first order model. Comparing both first and second order fitting trends, it is apparent that the second order model is more realistic in predicting a_{ss} value as previously reported for other catalytic systems [45]. Having confirmed the applicability of the GPLE to model the experimental deactivation profile, the next step was to de-convolute the total deactivation into that caused by sintering and coking, respectively. From a visual appraisal of the experimental deactivation profile, it is readily evident that deactivation in the monometallic catalyst is controlled differently compared to the bi-metallic catalytic system. Therefore deconvolution was performed following the method described by Argyle et al. [45].

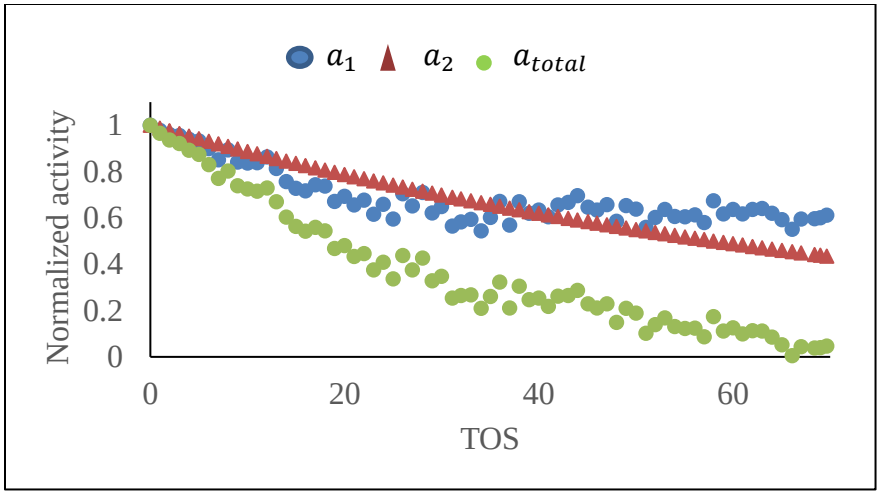

Figure 18: The fraction of activity loss due to sintering and carbon deposition in the Ni/ γ-Al_2O_3 catalyst, where a_1 is the activity profile due to the deactivation from sintering and a_2 is the activity profile due to the deactivation from carbon deposition.

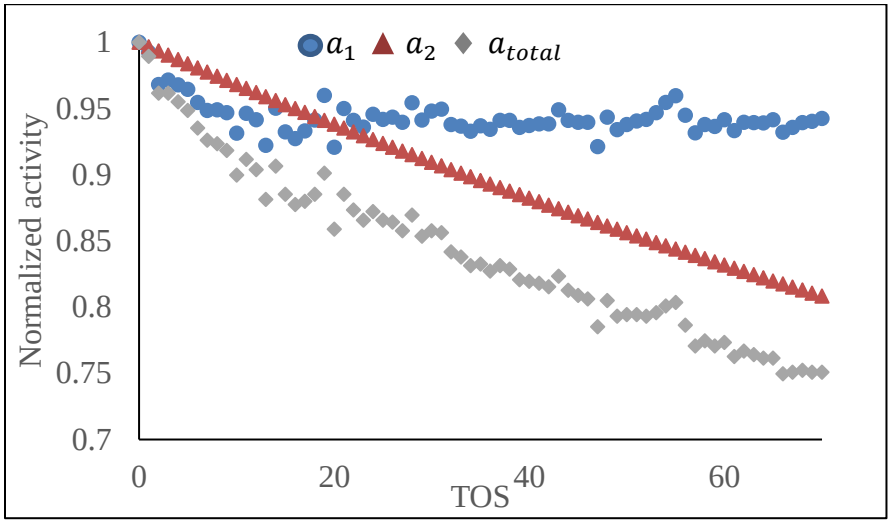

Figure 19: The fraction of activity loss due to sintering and carbon deposition in the Ni-Cu/ γ-Al_2O_3 catalyst.

Figure 18 and Figure 19 depicts the activity and fractional loss of activity for mono-metallic and bi-metallic catalyst over the TOS of 70 h. The fractional activity loss due to sintering is shown by f_1, and for the carbon deposition is shown by f_2 while the

total deactivation versus TOS is shown by f_{tot}. For the mono-metallic Ni/ γ-Al_2O_3 catalyst, the model results suggest that the sintering contribution in the total deactivation is negligible (<1%) while most of the deactivation is from carbon deposition. Therefore, to corroborate these results, TPO analysis of the spent catalyst is performed to determine the coke deposition.

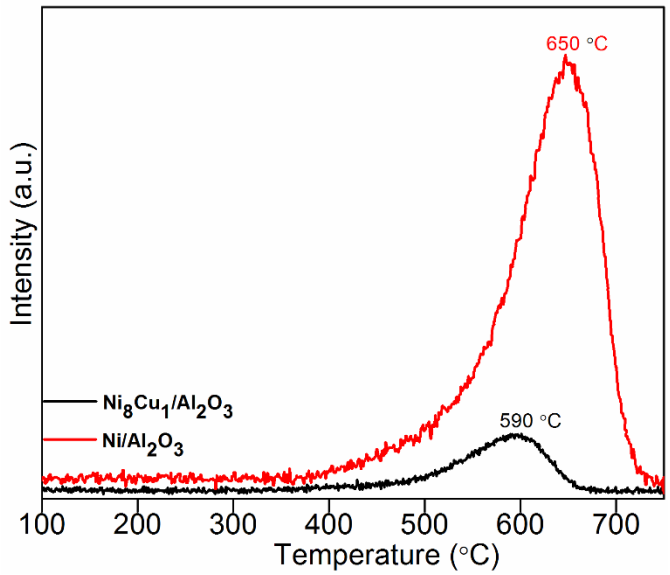

Figure 20: O_2-TPO profile of spent catalysts after DRM performance at 650 °C for 70h TOS

The TPO results (Figure 20) shows for the monometallic catalyst, graphitic type of carbon is produced from the intense CO_2 peak at 650 °C, while for bimetallic catalyst, amorphous type of carbon is produced at 590 °C. Also, the rate of carbon produced in the monometallic catalyst is much higher than the carbon produced in bimetallic catalyst, which is in agreement with the model results.

It was not possible to elucidate the model result in the sintering of the catalyst. Attempts to determine the sintering of the catalyst by calculating the dispersion loss using chemisorption study were unsuccessful on both the mono and bi-metallic spent catalysts. In contrast to the monometallic catalyst, deconvolution of the bi-metallic Ni_8Cu_1/Al_2O_3 catalyst data revealed that the ~77% of total deactivation loss is due to carbon deposition while 23% of activity loss due to sintering of the catalyst. One has to remember that these numbers correspond to a fraction of the total deactivation, which is still far lesser for the bi-metallic catalyst. Examining the literature, Wu. et al. [55] observes that the addition of Cu promotes the sintering resistance of a bimetallic Ni-Cu catalyst supported on silica nano-sheets. This is in contrast to the current study, wherein the modelling results are suggestive of a higher sintering contribution to the deactivation of the Ni-Cu bimetallic catalyst. However, the sintering occurs to a relatively lesser degree and, from experimental testing, does not appear to significantly impact the overall catalyst activity.

4.1.2. Commercial Catalyst Results

In this part, the industrial catalyst (Riogen 20% $Ni/\gamma\text{-}Al_2O_3$) deactivation profile at two different temperature 650 and 550 °C are compared.

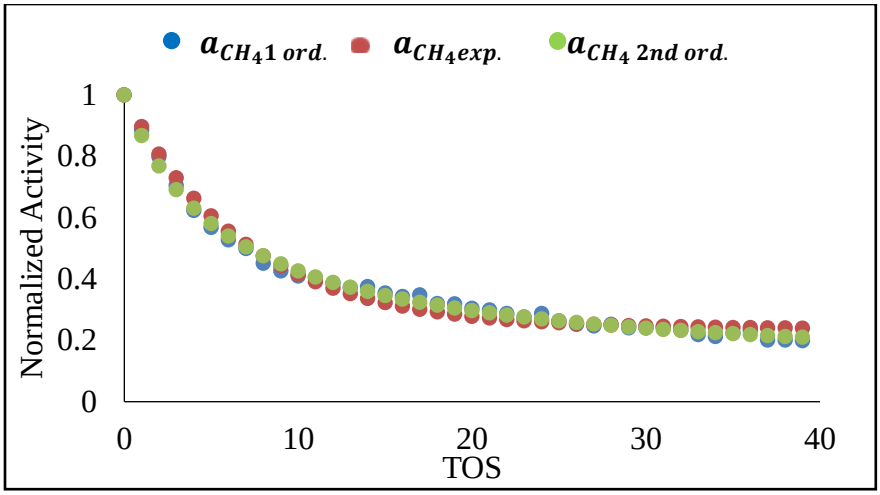

Figure 21: Activity versus TOS for Riogen catalyst in DRM reaction at 650 °C, 1 bar, CH_4/CO_2=1

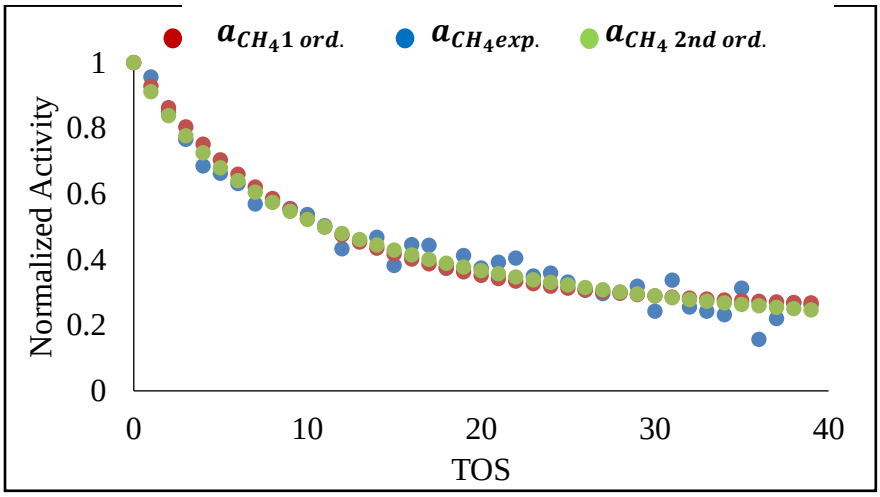

Figure 22: Activity versus TOS for Riogen catalyst in DRM reaction at 550 °C, 1 bar, CH_4/CO_2=1

Figure 21 shows the activity versus TOS for the Riogen catalyst at 650 °C over 40 h TOS. At 650 °C the first and second order GPLE have same trend lines with R^2 values of 0.98 and 0.99, respectively. However, the calculated SSA value for the two models is notably different with 0.24 for the first order model and 0.09 for the second order model. Again, the second order GPLE shows lower SSA than the first order, which is previously

reported for other catalytic systems [45]. For the Riogen catalyst at 550 °C (Figure 22) the deactivation profile appropriately fits first and second order GPLE with R^2 values of 0.96 and 0.97, while the predicted SSA values are 0.25 and 0.06, respectively. Since the reaction temperature for the two catalysts was 100 °C different and the predicted SSA was to some extent similar, we can say that the effect of temperature in this study is not revealed.

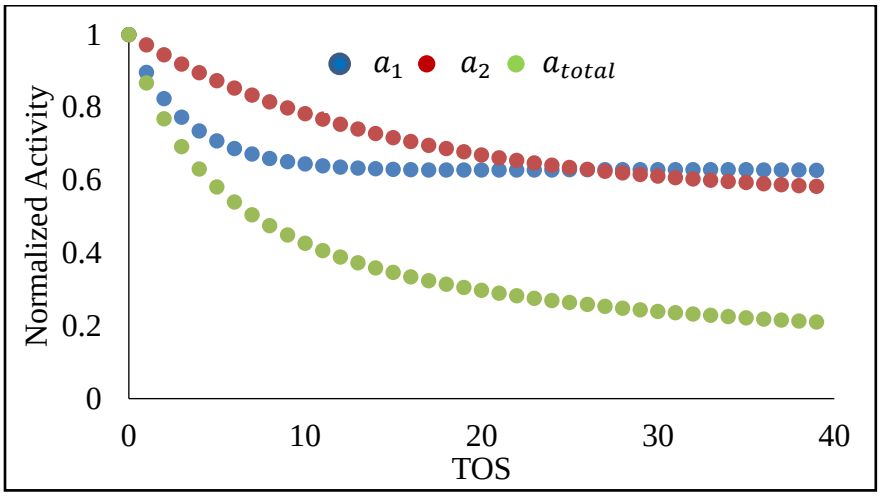

Figure 23: The fraction of activity loss due to sintering and carbon deposition in the Riogen 650 °C catalyst

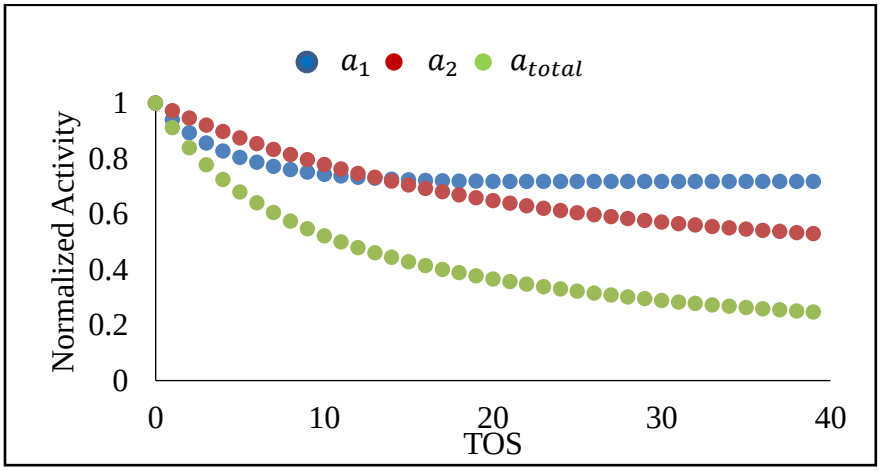

Figure 24: The fraction of activity loss due to sintering and carbon deposition in the Riogen 550 °C catalyst

The deconvolution results for the Riogen tested for the DRM at 650 and 550 °C are shown in Figure 23 and Figure 24, respectively. In the Riogen tested at 650 °C (Figure 23), the predicted contribution of the deactivation from sintering from the total activity loss varies from 53 % at 40 h TOS to 47% at infinity TOS. Deactivation from carbon deposition starts with slow deactivation rate until it reaches 53% of the total activity loss at infinite TOS. For the Riogen tested at 550 °C (Figure 24) the model results revealed that 37 % of total activity loss is due to sintering, while 63% of the total deactivation is due to carbon deposition. Since the total activity loss for both catalysts are somehow equal, and the percentage of the activity loss from carbon deposition is higher in 550 °C than 650 °C , these show that at a higher temperature the contribution of carbon deposition is less which is noticed in the literature [56].

4.1.3. Atomic Layer Deposition (ALD) Catalyst Results

In this part, the deactivation profile for the 20% Ni/γ-Al_2O_3 catalyst cover with different layers of alumina overcoat (ALD1, ALD5, and ALD20) is investigated.

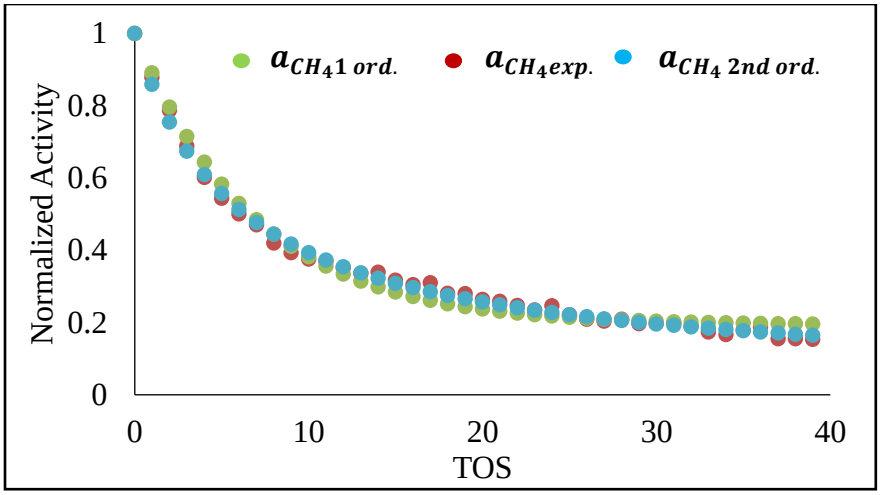

Figure 25: Activity versus TOS for 1-ALD catalyst in DRM reaction at 650 °C

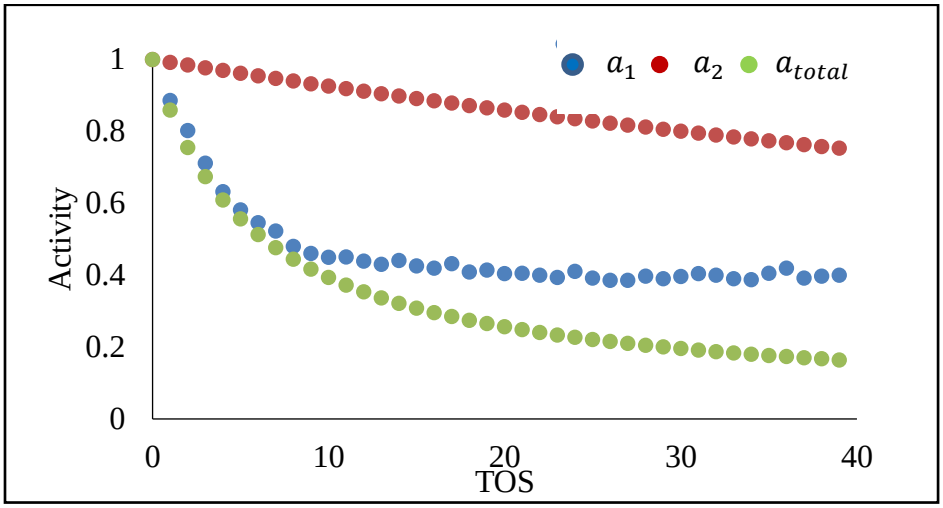

Figure 26: The fraction of activity loss due to sintering and carbon deposition in 1-ALD catalyst in DRM reaction at 650 °C

Figure 25 shows the activity versus TOS for 20% Ni/γ-Al_2O_3 catalyst covers with one layer of pores alumina sheet at 650 °C over 40 h TOS. The first and second order GPLE fitting results match perfectly to the experimental data with R^2 values of 0.98 and 0.99 respectively. The calculated SSA for the first order GPLE is 0.19 while the SSA for the second order is 0.04 which is repeatedly less than the first order SSA. When we come

to the mechanism deconvolution (Figure 26) the model results predict that 52% of the total deactivation is coming from the sintering while 48% is from the carbon deposition.

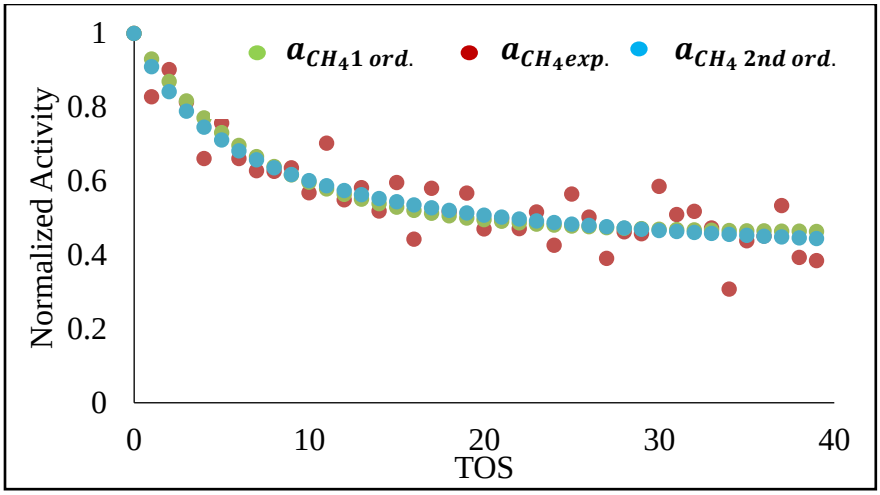

Figure 27: Activity versus TOS for 5-ALD catalyst in DRM reaction at 550°C

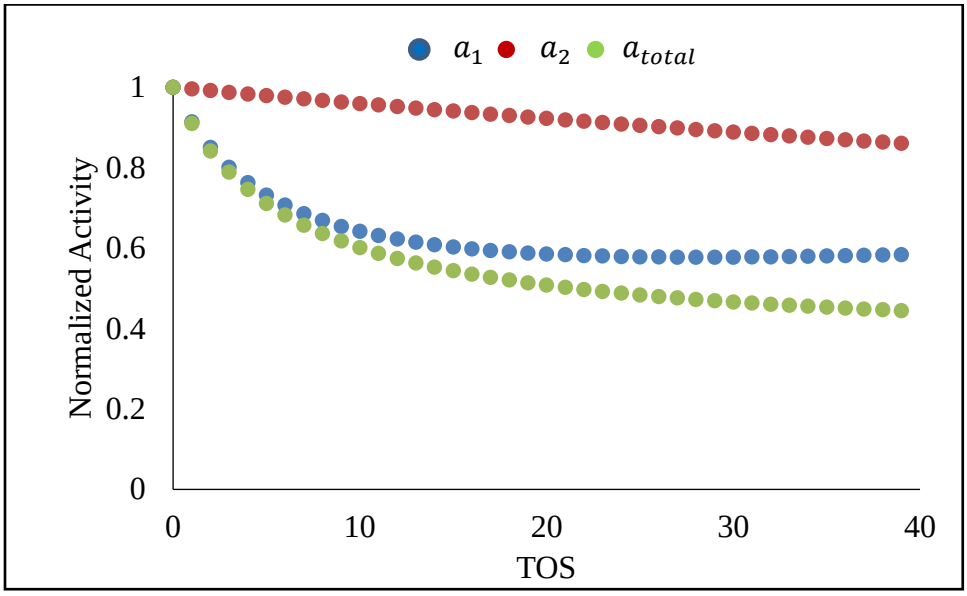

Figure 28: The fraction of activity loss due to sintering and carbon deposition in 5-ALD catalyst in DRM reaction at 550 °C

Figure 27 illustrates the activity versus TOS data for 20% Ni/γ-Al_2O_3 catalyst covers with five layers of pores alumina sheet at 550 °C over 40 h TOS. In this case,

although the first and second order models have a similar trend line, the coefficient of determination (R^2) for both models are 0.83 and 0.84, respectively. The calculated SSA is 0.46 for first order model and 0.36 for the second order model. The deconvolution results (Figure 28) predict that the percentage loss of the activity from sintering is varying from 75% at 40 h TOS to 50% at an infinite time while the percentage loss of activity from carbon deposition is varying from 25% at 40 h TOS to 50 % at infinity TOS.

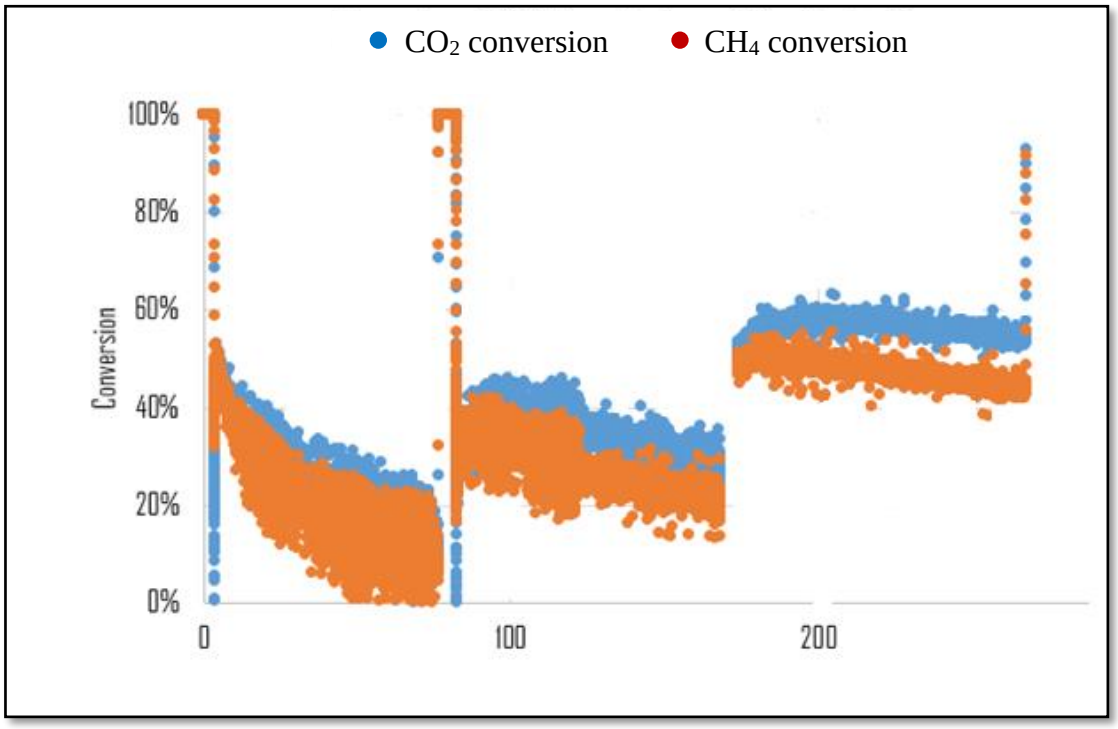

Figure 29: Experimental data for the 20-ALD

For the 20-ALD cycle, the obtained experimental data was for 600 TOS. The catalyst exposed to temperature programmed oxidation (TPO) at 800 °C periodically after 80 h TOS to remove the deposited carbon from the catalyst surface. So, we divided the total TOS data for 80 h interval

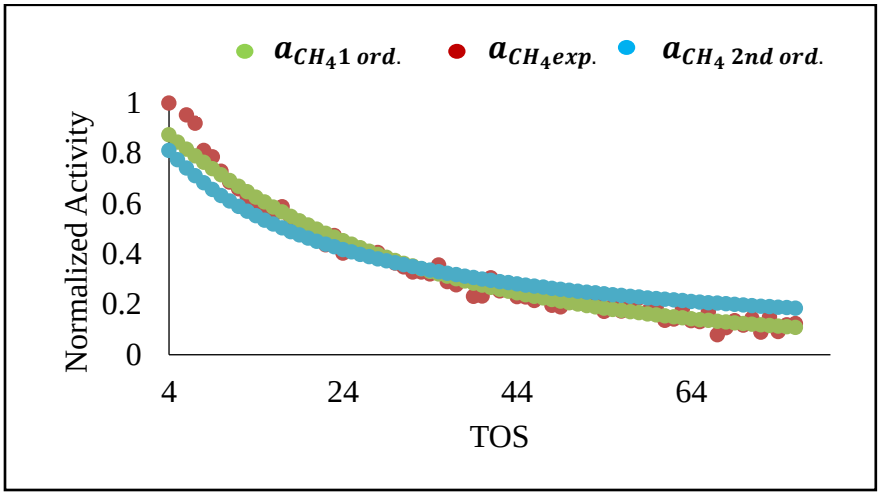

Figure 30: Activity versus TOS for 20-ALD catalyst in DRM reaction at 650°C, (0-80 h) TOS

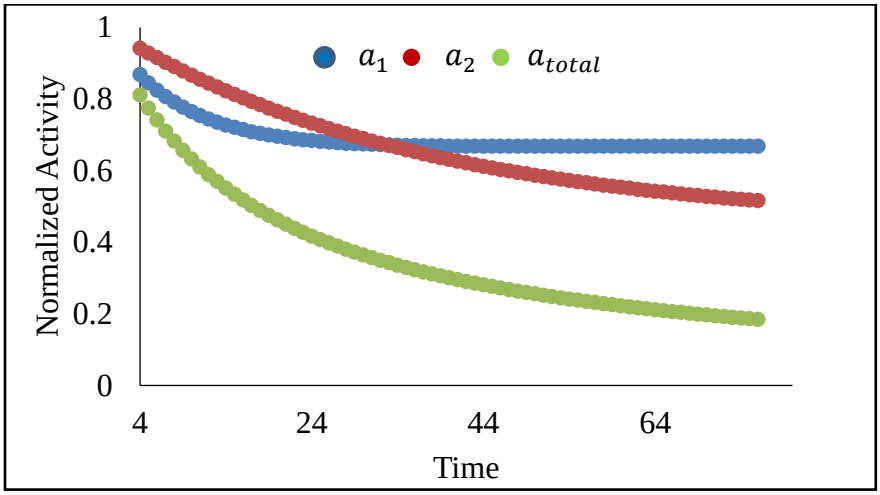

Figure 31: The fraction of activity loss due to sintering and carbon deposition in the 20-ALD catalyst in DRM reaction at 650 °C (0-80) TOS

Figure 30 and Figure 31 show the deactivation study result for the first interval (0-80 h) TOS for the 20 cycles ALD. The fitting results show that the first and second order GPLE model fit quite well with R^2 of 0.97 and 0.99 respectively, while the predicted SSA values are 0.04 for the first order and zero for the second order. Here again, we see a

contrast with the main assumption of the GPLE. The model results predict that 40% of the total activity loss is coming from sintering and 60% is from carbon deposition. The initial CH_4 conversion was 48%, and according to the model result, the catalyst is expected to lose almost all of activity after 80 h TOS. Since TPO was conducted after 80 h, the deactivation from carbon deposition are likely to despair and end up having just the deactivation from sintering that means the next interval conversion should start from 28.8 % (48×0.6) and it agrees with the experimental data (Figure 29).

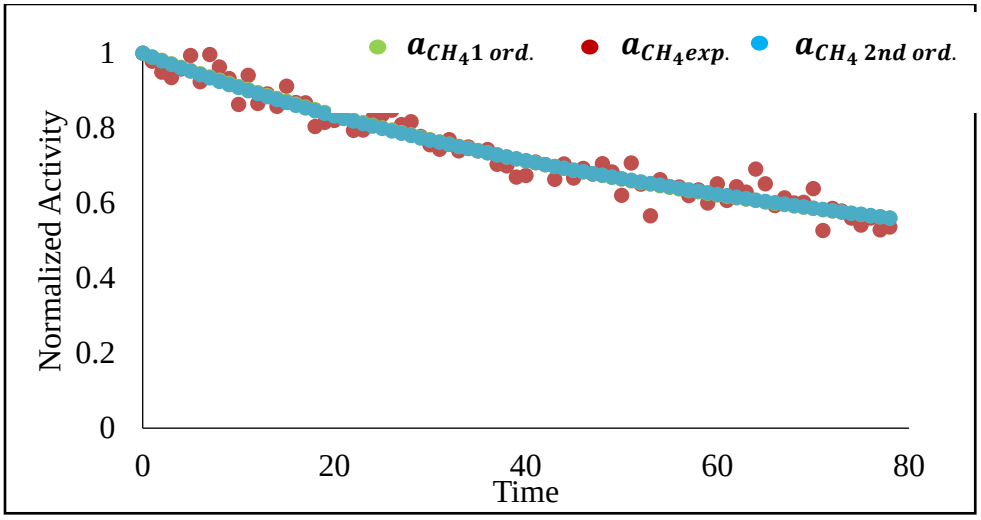

Figure 32: Activity versus TOS for 20-ALD catalyst in DRM reaction at 650 °C, (80-160 h) TOS

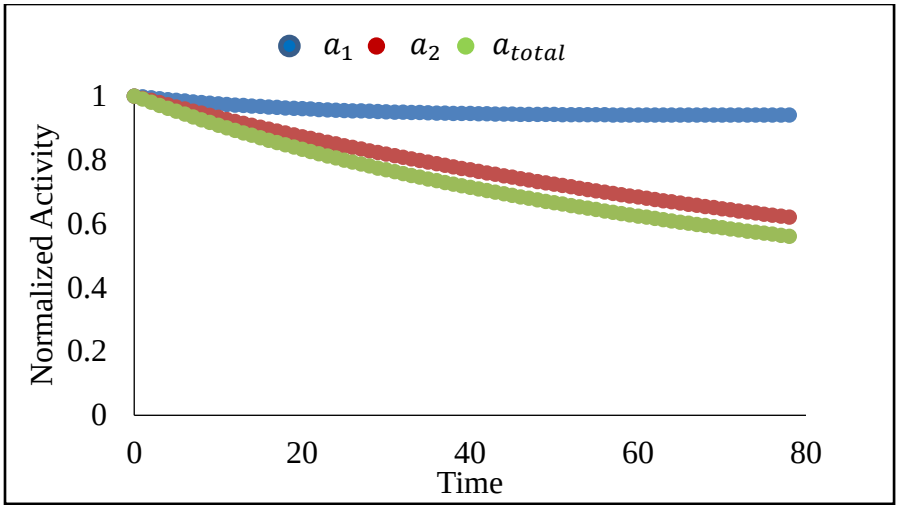

Figure 33: The fraction of activity loss due to sintering and carbon deposition in the 20-ALD catalyst in DRM reaction at 650°C (80-160) TOS

Figure 32 and Figure 33 elucidate the deactivation results for the second interval in the 20-ALD cycle. In this interval, the first order model fit the data slightly better than the second order with R^2 of 0.95 and 0.93, respectively. The predicted SSA values are 0.36 for the first order and zero for the second order. The mechanism deconvolution results (Figure 33) show that the total activity loss from sintering varies from 14% at 80 h TOS to 10% at infinite TOS while the activity loss from carbon deposition is varying from 86% at 80 h TOS to 90% at infinite TOS.

Table 3: The fitting results for the catalyst deactivation study

Catalyst	First order			Second order		
	K_d(1/h)	a_{ss}	R^2	K_d(1/h)	a_{ss}	R^2
Ni_8Cu_1/γ-Al_2O_3	0.029	0.725	0.965	0.061	0.615	0.965
Ni/γ-Al_2O_3	0.036	0	0.981	0.066	0	0.955
Riogen (650 °C)	0.146	0.237	0.985	0.189	0.092	0.995
Riogen (550 °C)	0.101	0.254	0.961	0.111	0.060	0.972
ALD-5 (550 °C)	0.138	0.461	0.826	0.254	0.357	0.838
ALD-1 (650 °C)	0.146	0.193	0.985	0.178	0.040	0.996

Table 4: The mechanism deconvolution results

Catalyst	Rapid deactivation (Sintering)			Slow deactivation (C deposit)			Mechanism contribution
	TOS (h)	K_d(1/h)	a_{ss},fast	TOS(h)	K_d(1/h)	a_{ss},slow	
Ni_8Cu_1/γ-Al_2O_3	0-30	6.95	0.94	30-72	0.005	0.36	Sintering (23%) C deposit (77%)
Ni/γ-Al_2O_3	0-30	0.13	0.99	30-70	0.01	0.01	Sintering (1%) C deposit (99%)
Riogen (650 °C)	0-15	1.231	0.595	15-39	0.066	0.548	Sintering (47%) C deposit (53%)
Riogen (550 °C)	0-20	1.057	0.683	20-39	0.053	0.461	Sintering (37%) C deposit (63%)
ALD-5 (550 °C)	0-20	0.568	0.522	20-39	0.009	0.512	Sintering (50%) C deposit (50%)
ALD-1 (650 °C)	0-20	0.902	0.518	20-39	0.059	0.560	Sintering (52%) C deposit (48%)

4.2. Modelling of Catalyst Selectivity Results

This section discusses the results obtained from the experimental campaign. The experimental campaign was designed to cover the FTS performance in the critical and near critical operation. To understand the effect of the position in the supercritical regime, six experimental runs were maintained in the reactor, as shown in Figure 34 and Table 5: Experimental conditions and alpha value:

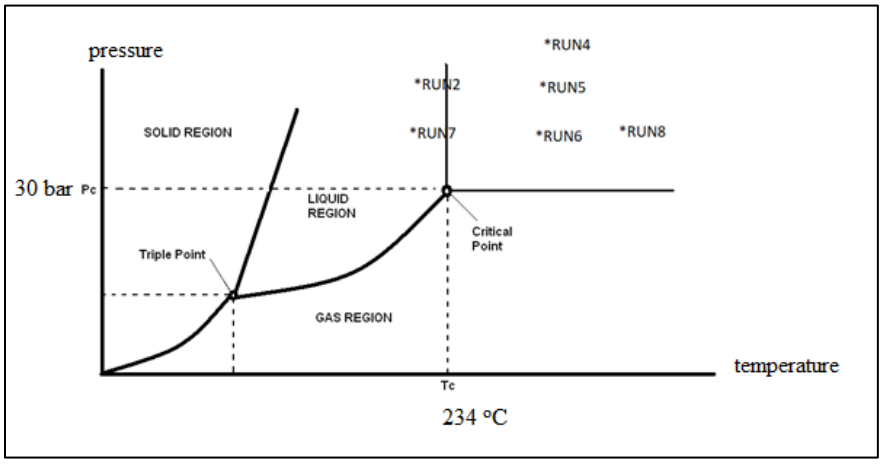

Figure 34: Experimental conditions

Table 5: Experimental conditions and alpha value

Run No.	Temperature (°C)	Pressure (bar)	α-3 Value
1	230	45	0.97
2	230	65	0.931
3	240	80	0.839
4	240	65	0.911
5	240	45	0.986
6	250	45	0.787

4.2.1. SCF-FTS Reaction Performance

The reactor was running for a total of 537 h time on stream (TOS). For each run, the product distribution was determined by analyzing the wax, liquid and gas samples. In

this section, only the fifth run data will be discussed. The other five runs exhibit similar trends in terms of product distributions.

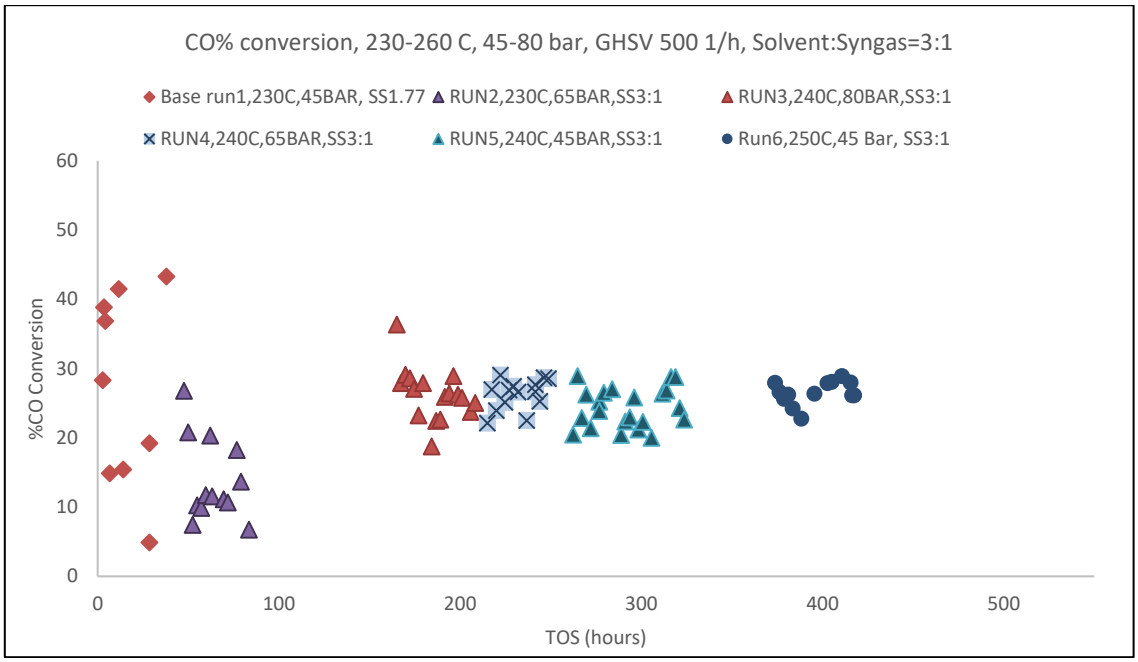

Figure 35: CO conversion % with TOS

The % CO conversion varied between 45-5% with variation in pressure and temperature, as shown in Figure 35. The % CO conversion for run 1 and 2 did not follow any consistent pattern and further decreased on increasing the pressure. In run 1 and 2, the reaction conditions were moderate in terms of temperature to operate the reactor under near-critical conditions. Therefore, more wax condensed on the catalyst surface and blocked the catalyst access for the reactive gases and therefore run 1 and run 2 resembles a gas phase FTS behavior. However, further increasing temperature to 240°C, the reactor was operating under the near critical or super critical conditions. This is evident from the next four runs as depicted in Figure 35, where a constant % CO was obtained. This is due to the fact that the supercritical hexane was cleaning the catalyst surface in situ and

therefore, the catalyst did not suffer any activity loss due to wax condensation. It is also important to note that variation in the pressure from 45-80 bar in runs 3-6 did not reveal any significant % CO conversion.

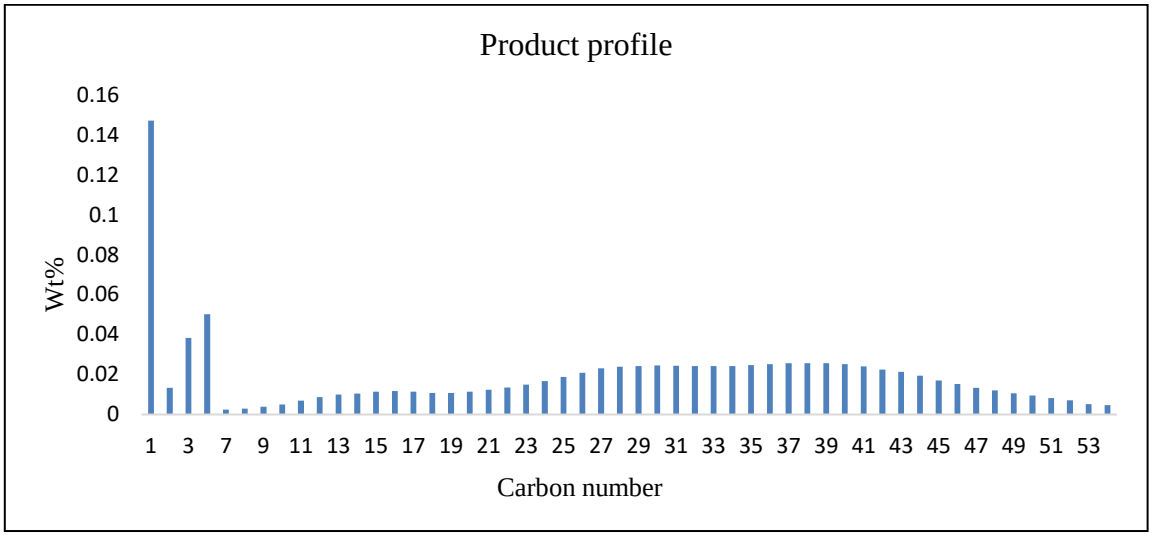

Figure 36: Product distribution for run 5

The product distribution for the wax sample in run 5 is shown in Figure 36. The hexane and pentane weight percent data were removed from the figure. This was mainly done since the SC reaction media (hexane) contained pentane as an impurity. The peaks area for C_1-C_7 was calculated from the on-line analysis while the hydrocarbons formation rates higher than C_7 were estimated from the off-line analysis. The GC peak up to C_{53} were identified for run 5 hinting a higher chain growth probability for this run.

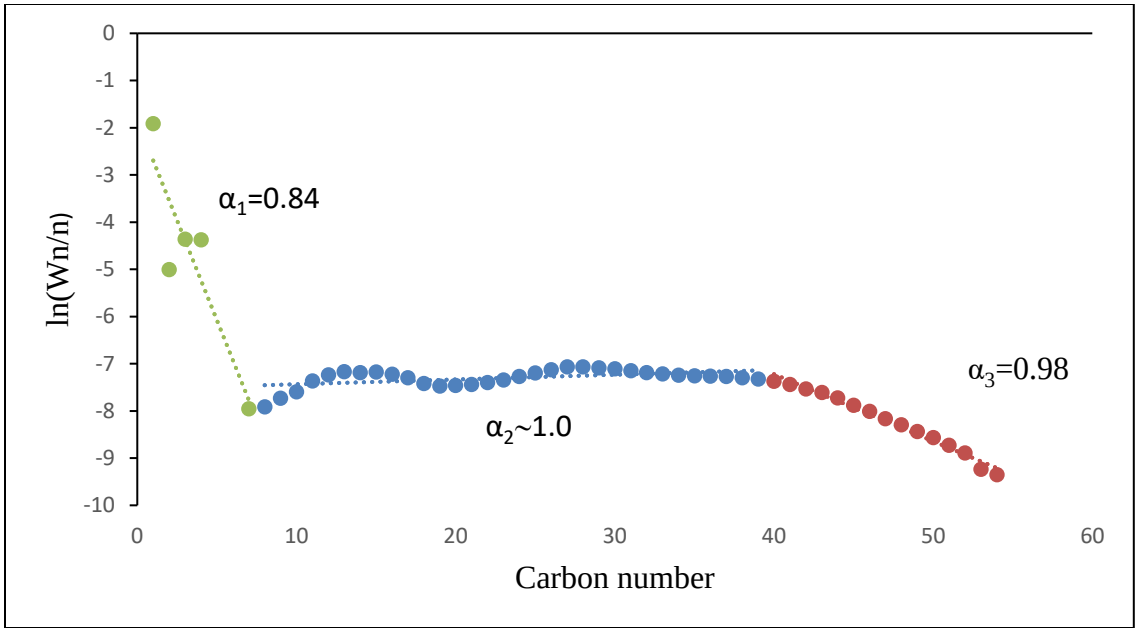

Figure 37: ASF plots for run 5

As mentioned previously, the ideal ASF product distribution follows a straight line with a single α value. As shown in (Figure 37), the experimental data shows a deviation from the ideal ASF model, especially in the range C_1-C_7. The deviation in C_2 is assumed to be mainly from the 1-olefin reabsorption as reported in the literature. However, the extended deviation in the ASF plot in the SCF-FTS runs are due to olefin re-adsorption and thereby increasing α-value for the reaction. The saddle-like ASF plot obtained for this run also hints that the reactor was running under SCF-FTS condition. The ASF plot for the run gave three α-value (α_1 for C_1-C_7, α_2 for C_8-C_{40}, and α3 for C_{40}-C_{52}) which are also reported in the literature [57].

4.2.2. Model Results

The data obtained from the experiment was used to estimate model parameters of the developed GA code in MATLAB. The estimated model parameters from the GA are listed in Table 6

Table 6: Estimated model parameter from GA

Pre-exponential terms			Heat of reaction (kJ/mol)		Activation energy (kJ/mol)	
A_1	2.67E-01	bar $^{-1}$	ΔH_{r1}	-58.916	E_6	63.4885
A_2	5.93E-12	bar $^{-1}$	ΔH_{r2}	-64.694	E_7	133.022
A_3	9.83E-16	-	ΔH_{r3}	-76.382	E_8	67.510
A_4	3.09E+04	-	ΔH_{r4}	-39.033	E_9	97.081
A_5	1.48E-08	-	ΔH_{r5}	-12.103	E_{10}	116.887
A_6	7.09E+04	mol/g_{cat}/h			E_{11}	118.885
A_7	4.33E+08	mol/g_{cat}/h			ΔE	6.45
A_8	1.96E+01	mol/g_{cat}/h				
A_9	4.75E+06	mol/g_{cat}/h				
A_{10}	3.79E+07	mol/g_{cat}/h				
A_{11}	2.58E-15	mol/g_{cat}/h				

The MARR was used to check the model fitness. The maximum value for the MARR was 35.32%. The adsorption is an exothermic reaction; thus, the heat of adsorption must be negative. The heat of adsorption of hydrogen (ΔH_{r1}) was -58.916 kJ/mol, which is similar to the reported value of -43 kJ/mol for supported cobalt catalyst [58]. All the estimated activation energies are positive since they should obey the Arrhenius equation and varied from 63-134 kJ/mol.

Figure 38 shows the formation rate, the ASF plot, and the olefin to paraffin ratio for run one. According to Figure 38, the model was able to predict the paraffin formation rate more accurately than the olefin formation rate. In

Figure 38, the olefin formation rate was under predicted, this could be attributed to contribution from olefin re-adsorption theory. Also, the activation energy of the paraffin termination (E8) is less than the activation energy of both chain growth (E7) and olefin termination (E9). As a result, the formation rate of the paraffin is more favored. Moreover, the olefin activation energy (E9) is slightly less than the predicted value of Todic et el. [41]. The model was able to predict the product distribution as evident from Figure 38, that provided a comparison between the experimentally measured and the modeled ASF distribution. The calculated ASF product distribution obtained from the model shows three α-values, which agrees with the experimental data but a significant deviation from the experimental data was observed for the light hydrocarbon product distribution (i.e., C_3-C_5 range). The predicted olefin to paraffin ratio perfectly matched the experimental data on run 2 but there was limited deviation in C_3-C_5 carbon range in run 6, and C_8-C_{12} in run 1.

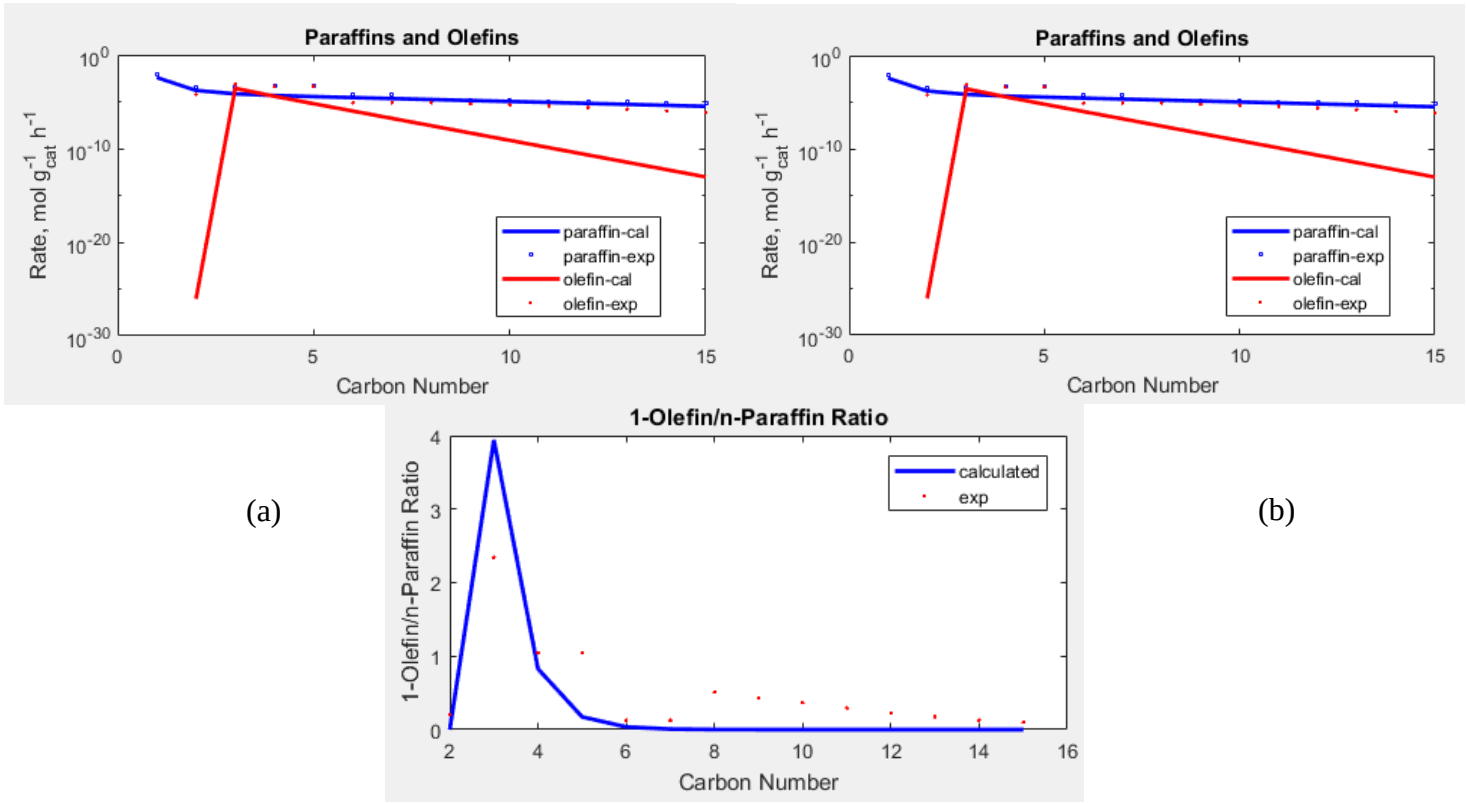

Figure 38: Comparison between the experimental and calculated product distribution for T= 230 ℃ , P=45 bar

4.2.3. Comparison Between the Model Results and the Reported Results in the Literature

The developed kinetic model shows that the maximum MARR value for the fitted data was 35.32% which is comparatively higher than the calculated MARR value by Todic et al. [41] in the slurry phase reaction (21.2%) and less than the predicted value by Afzal in the gas phase reaction (48.44%). This shows that the model results required more improvement to reduce the error.

The estimated activation energy to produce the paraffin (E_8=67.510 kJ/mol) in the developed SCF model is less than the predicted activation energy to produce the paraffin in the slurry phase reaction by Todic et al. [41] which is equal (72.4 kJ/mol). Since the SCF model was able to predict the paraffin formation rate fairly, that reflect the ability of the supercritical media to produce the paraffin easily than in the slurry phase reaction. However the predicted activation energy to produce the olefin (E_9) in the SCF phase model is equal to the reported olefin activation energy by Todic et al. [41] in the slurry phase reaction. Since our model was underestimated the olefin formation rate, this reflect the olefin formation rate is much higher in the SCF phase than in the slurry phase.

5. CONCLUSIONS AND FUTURE WORK

This study provided a framework to model the catalyst behavior both in terms of activity and selectivity for the GTL process. The modeling part focused on two of the major units in the GTL plant, which are the methane reformer unit and the Fischer Tropsch reactor. Also, the developed models proof accurate for different catalytic systems and at different operating conditions.

First, in the catalyst deactivation study, the GPLE model was used to predict the deactivation mechanism and the activity profile for different catalytic systems used in the dry reforming of methane (DRM) reaction. Almost all the experimental data in this study fitted well to the first and second GPLE models with regression factor (R^2) value ranged between 0.95 and 0.99. Furthermore, the study was able to predict the fraction loss of the activity from sintering and carbon deposition for all the catalytic systems. In the bimetallic and monometallic catalysts, the results indicate that the rapid deactivation of monometallic catalyst is primarily due to significant coke formation whereas, the bimetallic catalyst experienced minimal deactivation owing to both particle sintering in the initial phases followed by coke formation. In the commercial catalyst (Riogen) the model results indicate that at 550 °C the percent of activity lost due to carbon deposition is higher than the case for the catalyst tested for DRM at 650 °C, which agree well with the literature. While for the case of the ALD coated catalyst, the ALD-1 (one cycle coat) and ALD -5 (five cycles coat) model results indicate almost equal contribution from both sintering and coke deposition. The ALD-20 (twenty coated cycles) model results also have contribution

from both sintering and coke deposition in the first interval (0-80 TOS), but the contribution from sintering is negligible in the second interval (80-160 TOS) compared to the carbon deposition. These results are currently validated by experimental characterization of each spent sample (after the reaction) to confirm the contribution of each deactivation type and will be compared with the model results.

The second part of this thesis was focused on modeling the Fischer Tropsch catalyst selectivity for the non-conventional supercritical fluid reaction media. The study included; the development of detailed kinetics model based on the alkyl mechanism that is needed to model the hydrocarbon product distribution of the SCF-FTS. In order to account for the non-ideality of the system, the activity coefficient has been used as a correction factor for the intermediate concentration of the reactants and the products. To estimate the model parameters, six experimental runs campaign have been carried out in the high-pressure multi-purpose reactor unit at Texas A&M University at Qatar Fuel Characterization Laboratory. Besides using the experimental data to verify the predictability of the hydrocarbon product distribution developed model it was used as an input for genetic algorithm code in MATLAB. The model results show that the maximum MARR for the fitted data was 35.32%. Also, the model was able to predict the product distribution trend line fairly Nevertheless, the model was underestimated the olefin formation rate because of the olefin re-adsorption theory that used and also, the alkyl mechanism that used to represent the reaction network gives an advantage for the paraffin formation rather than the olefin formation, thus it underestimates the olefin selectivity.

Based on the outcome of this research work, the followings topics are recommended as an extension of this study and for future work to develop more accurate models for the GTL reactors and for catalysis in general:

1. The DRM reaction runs at high temperature that can reach up to 1000℃. However, in this study the Ni-based catalysts were tested at two different temperatures (550 and 650 ℃), therefore the activation energy for the deactivation cannot be determined. In order to predict the change in the activity at different temperatures, a detailed study that covers a wider range of temperatures is required.
2. In the GPLE model used to predict the catalyst activity, the effect of reactant and product concentrations on the deactivation profile was not considered. To improve the accuracy of model prediction, a GPLE model that accounts for the reactant and product concentrations should be developed.
3. Seven experimental runs were used to predict the kinetic parameters of the SCF-FTS reaction; however, All the experimental runs were conducted at constant CO and H_2 partial pressures. More experimental data at different reactant partial pressures and temperatures is required to improve the model results.
4. In the SCF-FTS kinetic model, the regular solution theory was used to calculate the activity coefficient assuming a binary mixture (CO and H_2) to simplify the complexity of the model calculation. However, the interaction between all the products involved in the SCF-FTS reaction should be considered.

REFERENCES

[1] O. Glebova, Gas to liquids: Historical development and future prospects, no. November. The Oxford Institute for Energy Studies, 2013.

[2] M. A. Marvast, M. Sohrabi, S. Zarrinpashne, and G. Baghmisheh, “Fischer-Tropsch synthesis: Modeling and performance study for Fe-HZSM5 bifunctional catalyst,” Chem. Eng. Technol., vol. 28, no. 1, pp. 78–86, 2005.

[3] I. Onwukwe Stanley, “Gas-to-Liquid technology: Prospect for natural gas utilization in Nigeria,” J. Nat. Gas Sci. Eng., vol. 1, no. 6, pp. 190–194, 2009.

[4] M. E. Dry, “Practical and theoretical aspects of the catalytic Fischer-Tropsch process,” Appl. Catal. A Gen., vol. 138, no. 2, pp. 319–344, 1996.

[5] S. Afzal, D. Sengupta, A. Sarkar, M. El-Halwagi, and N. Elbashir, “Optimization approach to the reduction of CO 2 emissions for Syngas Production involving dry reforming,” ACS Sustain. Chem. Eng., vol. 6, no. 6, pp. 7532–7544, 2018.

[6] R. Snel, “Olefins from syngas,” in Catalysis Reviews, vol. 29, no. 4, Catalysis Reviews Science and Engineering ISSN:, 1987, pp. 361–445.

[7] F. Duchézeau, “RATP’s commitment to sustainable development,” Public Transp. Int., vol. 52, no. 5, p. 27, 2003.

[8] S. Arora and R. Prasad, “An overview on dry reforming of methane: Strategies to reduce carbonaceous deactivation of catalysts,” RSC Adv., vol. 6, no. 110, pp. 108668–108688, 2016.

[9] C. Price, E. Earles, L. Pastor-Pérez, J. Liu, and T. Reina, “Advantages of yolk

shell catalysts for the DRM: A Comparison of Ni/ZnO@SiO2 vs. Ni/CeO2 and Ni/Al2O3," Chemistry (Easton)., vol. 1, no. 1, pp. 3–16, 2018.

[10] C. H. Bartholomew and R. J. Farrauto, fundamentals of industrial catalytic processess, Second edi. Wiley-interscience, 2006.

[11] P. R. K. Fu, F. Twaiq, and W. L. Chung, "Microkinetic deactivation studies on nickel supported catalyst for dry reforming of methane," IOP Conf. Ser. Mater. Sci. Eng., vol. 429, no. 1, 2018.

[12] F. Banisharifdehkordi and M. Baghalha, "Catalyst deactivation in industrial combined steam and dry reforming of natural gas," Fuel Process. Technol., vol. 120, pp. 96–105, 2014.

[13] C. H. Bartholomew, "Sintering kinetics of supported metals: new perspectives from a unifying GPLE treatment," Appl. Catal. A, Gen., vol. 107, no. 1, pp. 1–57, 1993.

[14] D. Operasi, "Prediction of industrial catalysts deactivation rate using first principle model and operating data," Malaysian J. Anal. Sci., vol. 21, no. 1, pp. 204–212, 2017.

[15] V. Pawar, D. Ray, C. Subrahmanyam, and V. M. Janardhanan, "Study of short-term catalyst deactivation due to carbon deposition during biogas dry reforming on supported Ni catalyst," Energy and Fuels, vol. 29, no. 12, pp. 8047–8052, 2015.

[16] H. A. Choudhury, X. Cheng, S. Afzal, A. V Prakash, B. J. Tatarchuk, and N. O. Elbashir, "Understanding the deactivation process of a microfibrous entrapped

cobalt catalyst in supercritical fluid Fischer-Tropsch synthesis," Catal. Today, no. 1, 2019.

[17] Y. Zhao, Y. Kang, H. Li, and H. Li, "CO2 conversion to synthesis gas: Via DRM on the durable Al2O3/Ni/Al2O3 sandwich catalyst with high activity and stability," Green Chem., vol. 20, no. 12, pp. 2781–2787, 2018.

[18] H. Lee, "Optimization of Fischer-Tropsch plant," Univ. Manchester, pp. 1–267, 2010.

[19] X. Lu, "Fischer-Tropsch synthesis : towards understanding," University of the Witwatersrand, 2011.

[20] J. Edgar and D. Ii, "Supercritical fluids for Fischer Tropsch synthesis and related reactions," Auburn University, 2011.

[21] K. Fujimoto, "Supercritical phase synthesis reaction," Fuel, vol. 68, pp. 255–256, 1989.

[22] B. Subramaniam, "Enhancing the stability of porous catalysts with supercritical reaction media," Appl. Catal. A Gen., vol. 212, no. 1–2, pp. 199–213, 2001.

[23] A. Kasht, "Experimental validation of a novel fischer-tropsch tubular fixed bed reactor under conditions," Texas A&M University, 2015.

[24] G. Jacobs et al., "Fischer-Tropsch synthesis: Supercritical conversion using a Co/Al2O3 catalyst in a fixed bed reactor," Fuel, vol. 82, no. 10, pp. 1251–1260, 2003.

[25] X. Huang and C. B. Roberts, "Selective Fischer-Tropsch synthesis over an Al2O3supported cobalt catalyst in supercritical hexane," Fuel Process. Technol.,

vol. 83, no. 1-3 SPEC., pp. 81–99, 2003.

[26] D. B. Bukur, X. Lang, and L. Nowicki, “Comparative study of an iron fischer-Tropsch catalyst performance in stirred tank slurry and fixed-bed reactors,” Ind. Eng. Chem. Res., vol. 44, no. 16, pp. 6038–6044, 2005.

[27] C. K. Rofer-DePoorter, “A comprehensive mechanism for the Fischer-Tropsch synthesis,” Chem. Rev., vol. 81, no. 5, pp. 447–474, 1981.

[28] N. Moazami, M. L. Wyszynski, K. Rahbar, A. Tsolakis, and H. Mahmoudi, “A comprehensive study of kinetics mechanism of Fischer-Tropsch synthesis over cobalt-based catalyst,” Chem. Eng. Sci., vol. 171, pp. 32–60, 2017.

[29] R. C. Brady and R. Pettit, “Mechanism of the Fischer-Tropsch reaction. The chain propagation step,” J. Am. Chem. Soc., vol. 103, no. 5, pp. 1287–1289, 1981.

[30] L. S. Fernandes and M. A. Peres, “Associação entre atenção básica em saúde bucal e indicadores socioecon_comicos municipais,” Rev. Saude Publica, vol. 39, no. 6, pp. 930–936, 2005.

[31] N. Moazami, M. L. Wyszynski, K. Rahbar, A. Tsolakis, and H. Mahmoudi, “A comprehensive study of kinetics mechanism of Fischer-Tropsch synthesis over cobalt-based catalyst,” Chem. Eng. Sci., vol. 171, pp. 32–60, 2017.

[32] B. Todic, “Kinetic modeling and optimization of fixed-Bed reactor for Fischer-Tropsch synthesis” university of Belgrade, 2015.

[33] Y. Wang et al., “Kinetics modelling of Fischer –Tropsch synthesis over an industrial Fe –Cu– K catalyst,” Fuel, vol. 82, pp. 195–213, 2003.

[34] B. H. Davis, “Fischer-Tropsch Synthesis: reaction mechanisms for iron catalysts,”

Catal. Today, vol. 141, no. 1–2, pp. 25–33, 2009.

[35] R. Snel, “Deviations from ASF,” vol. 1, J.C Baltzer A.G Scientific Puplishing Compony, 1988, pp. 327–330.

[36] B. H. Davis, “The two-alpha value for iron Fischer-Tropsch catalysts: fact or fiction?,” Prepr. Pap. - Am. Chem. Soc., vol. 37, no. 1, pp. 172–183, 1992.

[37] N. Elbashir, D. Bukur, E. Durham, and C. Roberts, “Advancement of Fischer-Tropsch synthesis via utilization of supercritical fluid reaction media,” AIChE J., no. DOI 10.1002/aic.12032, 2009.

[38] D. J. Bochniak and B. Subramaniam, “Fischer-Tropsch synthesis in near-critical n-hexane: pressure-tuning effects,” AIChE J., vol. 44, no. 8, pp. 1889–1896, 1998.

[39] A. Sangalli, “Why Sales Representative Pose a Hard Problem,” New Scientist, 12, vol. 136, no. 1851. pp. 24–28, 1992.

[40] A. K. Mogalicherla and N. O. Elbashir, “Development of a kinetic model for supercritical fluids fischer-tropsch synthesis,” Energy and Fuels, vol. 25, no. 3, pp. 878–889, 2011.

[41] B. Todic et al., “Kinetic model of Fischer-Tropsch synthesis in a slurry reactor on Co-Re/Al2O3 catalyst,” Industrial and Engineering Chemistry Research, vol. 52, no. 2. pp. 669–679, 2013.

[42] G. S. F. D. Planning, “Qatar National Vision 2030,” 2008.

[43] L. Joos et al., “Reactivity of CO on carbon-covered cobalt surfaces in fischer-tropsch synthesis,” J. Phys. Chem. C, vol. 118, no. 10, pp. 5317–5321, 2014.

[44] G. A. Fuentes, “Catalyst deactivation and steady-state activity: A generalized

power-law equation model," Appl. Catal., vol. 15, no. 1, pp. 33–40, 1985.

[45] M. D. Argyle, T. S. Frost, and C. H. Bartholomew, "Cobalt fischer-tropsch catalyst deactivation modeled using generalized power law expressions," Top. Catal., vol. 57, no. 6–9, pp. 415–429, 2014.

[46] A. Chatla, M. Ghouri, and N. Mohamed, "A Novel Approach to Design a Copper-Nickel Catalyst for CO2 Reforming Of Methane: experimental verification of DFT modeling capabilities in design of catalytic systems," 2019.

[47] P. Littlewood, S. Liu, E. Weitz, T. J. Marks, and P. C. Stair, "Ni-alumina dry reforming catalysts: Atomic layer deposition and the issue of Ni aluminate," Catal. Today, no. August 2018, pp. 0–1, 2019.

[48] F. Cansell, S. Rey, A. Thermodynamiques, and D. E. S. Proc$f$dfs, "Thermodynamic aspects of supercritical fluids processing : applications to polymers and wastes TREATMENT," vol. 53, no. 2, pp. 71–98, 1998.

[49] V. Barneveld and V. Ponec, "Reactions of CHJJ-, Fischer-Tropsch with Hydrogen: Relation to the Synthesis of hydrocarbons," J. Catal., vol. 387, pp. 382–387, 1984.

[50] R. Davarnejad, K. M. Kassim, A. Zainal, and S. A. Sata, "Thermodynamic model used to predict supercritical carbon dioxide separation of an ethanol-octane mixture: feasibility studies," int. J. Thermodyn., vol. 12, pp. 51–59, 2009.

[51] Z. Ahmad and R. Davarnejad, "Regular solution theory model used to Predict supercritical CO2 extraction of p- chlorophenol contaminate from water Stream."

[52] M. Mitchell, An introduction to genetic algorithms, first. massachusetts Institute

of Technology, 1998.

[53] K. Sastry, D. Goldberg, and G. Kendall, “Chapter 4 Genetic Algorithms,” Search Methodol., pp. 97–125, 2005.

[54] D. Beasley, D. R. Bull, and R. R. Martin, “An overview of genetic algorithms : Part 1, fundamentals,” Univ. Comput., vol. 2, no. 15, pp. 1–16, 1993.

[55] Z. Bian, S. Das, M. H. Wai, P. Hongmanorom, and S. Kawi, “A review on bimetallic Ni-Based catalysts for CO2 reforming of methane,” ChemPhysChem, pp. 3117–3134, 2017.

[56] V. Palma, F. Castaldo, P. Ciambelli, and G. Iaquaniello, “Hydrogen production through catalytic low-temperature bio-ethanol steam reforming,” Clean Technol. Environ. Policy, vol. 14, no. 5, pp. 973–987, 2012.

[57] N. O. Elbashir and C. B. Roberts, “Reaction pathway and kinetic modeling of Fischer-tropsch synthesis over an alumina supported cobalt catalyst in supercritical-hexane,” 2004.

[58] J. Zowtiak “The kinetics of H2 adsorption on and desorption from cobalt and the effects of support thereon,” Journal of Catalysis, vol. 83, no. 1. pp. 107–120, 2004.

APPENDIX A

DETAILED KINETICS MODEL CALCULATION

This section describes the detailed kinetics calculation for all the n-paraffin and 1-oleffen starting from C1-C15. The main assumptions and mechanism used in this calculation is already listed in section 3.2.1.

Formation rate of C_2:

1. Formation rate of ethane C_2H_6

$$C_2H_5.S + H.S \xrightarrow{k_{par}} C_2H_6 + 2S$$

$$R_{C_2H_6} = k_{par}[C_2H_5.S][H.S]$$

To calculate the rate of formation of ethane we assume quasi-steady-state theory for ($C_2H_5.S$)

$$\frac{d\,C_2H_5.S}{dt} = k_{pro}[CH_2.S][CH_3.S] - k_{par}[C_2H_5.S][H.S] - k_{olef2} * e^{2c}[C_2H_5.S] -$$

$$k_{pro}[CH_2.S][C_2H_5.S]$$

At steady state $\frac{d\,C_2H_5.S}{dt} = 0$

$$k_{pro}[CH_2.S][CH_3.S] = k_{par}[C_2H_5.S][H.S] + k_{olef2} * e^{2c}[C_2H_5.S] +$$

$$k_{pro}[CH_2.S][C_2H_5.S]$$

also

$$\alpha_2 = \frac{[C_2H_5.S]}{[CH_3.S]}$$

$$\alpha_2 = \frac{k_{pro}[CH_2.S]}{k_{par}[H.S]+k_{olef2}*e^{2c}+k_{pro}[CH_2.S]}$$

Finally:

$$R_{C_2H_6} = k_{par}\,\alpha_2[CH_3.S][H.S] = k_{par}\,\alpha_2\alpha_1[H.S]^2$$

2. Formation rate of ethane C_2H_4:

$$R_{C_2H_4} = k_{olef2} * e^{2c}[\,C_2H_5.S]$$

$$R_{C_2H_4} = k_{olef2} * e^{2c}[CH_3.S]\,\alpha_2$$

$$R_{C_2H_4} = k_{olef2} * e^{2c}\,\alpha_2\,\alpha_1[H.S]$$

So:

$$R_{C_2} = R_{C_2H_4} + R_{C_2H_6} = k_{par}\,\alpha_2\alpha_1[H.S]^2 + k_{olef2} * e^{2c}\,\alpha_2\,\alpha_1[H.S]$$

1. Formation rate of C_3H_8

$$C_3H_7.S + H.S \xrightarrow{k_{par}} C_3H_8 + 2S$$

$$R_{C_3H_8} = kpar[\,C_3H_7.S][H.S]$$

Material balance around $C_3H_7.S$:

$$\frac{d\,C_3H_7.S}{dt} = k_{pro}[CH_2.S][\,C_2H_5.S] - k_{par}[\,C_3H_7.S\,][H.S] - k_{olef} * e^{3c}[\,C_3H_7.S\,] -$$

$$k_{pro}[CH_2.S][\,C_3H_7.S\,] = 0$$

Using steady state assumption and chain growth probability definition:

$$\alpha_3 = \frac{k_{pro}[CH_2.S]}{k_{par}[H.S]+k_{olef}*e^{3c}+k_{pro}[CH_2.S]}$$

$$\alpha_3 = \frac{[\,C_3H_7.S\,]}{[\,C_2H_5.S]}$$

$$R_{C_3H_8} = k_{par}\,\alpha_3[\,C_2H_5.S][H.S] = k_{par}\,\alpha_3\alpha_2[CH_3.S][H.S] = k_{par}\,\alpha_3\alpha_2\alpha_1[H.S]^2$$

2. Formation rate of C_3H_6

$$C_3H_7.S \xrightarrow{kolef} C_3H_6 + H.S$$

$$R_{C_3H_6} = k_{olef} * e^{3c}[C_3H_7.S] = k_{olef} * e^{3c}\,\alpha_3\alpha_2\alpha_1\,[H.S]$$

$$R_{C_3} = R_{C_3H_8} + R_{C_3H_6}$$

$$R_{C_3} = k_{par}\,\alpha_3\alpha_2\alpha_1[H.S]^2 + k_{olef} * e^{3c}\,\alpha_3\alpha_2\alpha_1\,[H.S]$$

From this derivation we can see that we have two values for the chain growth probability factor:

$$\alpha_1 = \frac{[CH_3.S]}{[H.S]} = \frac{k_6[CH_2.S]}{k_{par1}[H.S] + k_{pro}[CH_2.S]}$$

$$\alpha_2 = \frac{[C_2H_5.S]}{[CH_3.S]} = \frac{k_{pro}[CH_2.S]}{k_{par}[H.S]+k_{olef2}*e^{2c}+k_{pro}[CH_2.S]}$$

$$\alpha_n = \frac{[C_nH_{2n+1}.S]}{[C_{n-1}H_{2n-1}.S]} = \frac{k_{pro}[CH_2.S]}{k_{par}[H.S]+k_{olef}*e^{nc}+k_{pro}[CH_2.S]} \qquad n > 2$$

Rate equations for hydrocarbons contain n carbon is:

$$R_{C_1} = k_{par1}\,\alpha_1[H.S]^2$$

$$R_{C_2} = k_{par}\,\alpha_2\alpha_1[H.S]^2 + k_{olef2} * e^{2c}\,\alpha_2\,\alpha_1[H.S]$$

$$R_{C_3} = k_{par}\,\alpha_3\alpha_2\alpha_1[H.S]^2 + k_{olef} * e^{3c}\,\alpha_3\alpha_2\alpha_1\,[H.S]$$

$$R_{C_n} = \prod_{i=1}^{n}\alpha_i\left[k_{par}[H.S]^2 + k_{olef} * e^{nc}[H.S]\right] \qquad n > 2$$

Calculation of intermediate's concentration:

The concentration of the hydrogen in the surface can be linked with the fraction of the vacant sites CV from the equilibrium relation;

$$K1 = \frac{[H.S]^2}{P_{H_2}CV^2\gamma_{H_2}}$$

$$[H.S] = \sqrt{K_1P_{H_2}\gamma_{H_2}}CV$$

The concentration of the monomer in the surface can be expressed in term of the partial pressure of the hydrogen and carbon monoxide using the equilibrium relationships:

$$K5 = \frac{[CH_2.S]CV}{[CH.S][H.S]}$$

$$[CH_2.S] = K_5[CH.S][H.S]\ /CV$$

$$K4 = \frac{[CH.S\ ]CV}{[C.S][[H.S]}$$

$$[CH_2.S] = K_5\ K_4[C.S][H.S]^2/CV^2$$

Calculation of carbon concentration on the surface:

We assume that the rate of oxygen removal is equal to the rate of carbon hydrogenation, from this assumption we can end up with:

$$[C.S] = [O.S]$$

And using the equilibrium relation:

$$K3 = \frac{[C.S][O.S]}{CV\ [CO.S]}$$

$$[\mathrm{C.S}] = \sqrt{\mathrm{K_3\ CV\ [CO.S]}}$$

$$K2 = \frac{[CO.S]}{CV\ P_{CO}\gamma_{CO}}$$

$$[CO.S] = K_2\ CV\ P_{CO}\ \gamma_{CO}$$

So: $[C.S] = \sqrt{K_3\ \ K_3\ \ P_{CO}\gamma_{CO}}CV$

From this equation we can calculate the monomer concentration as follow:

$$[CH_2.S] = K_5\ K_4[C.S][H.S]^2/CV^2 = K_5\ K_4\sqrt{K_3\ \ K_2\ \gamma_{CO}\ P_{CO}}K_1P_{H_2}\gamma_{H_2}CV$$

Determination of the fraction of the vacant sites:

The fraction of the vacancies and the occupied sites on the catalyst can be added to the unity. So, in order to calculate the fraction of the vacant sites we assume that the active radicals $[CH_2.S, CH.S]$ and water do not occupy a significant part of the active site.

There are we write the balance of the site as follows:

$$1 = CV + [CO.S] + [C.S] + [O.S] + [H.S]$$

$$1 = CV + K_2\ CV\ P_{CO}\ \gamma_{CO} \quad + 2\sqrt{K_3\ \ K_2\ \ P_{CO}\gamma_{CO}}CV \quad + \sqrt{K_1 P_{H_2}\gamma_{H_2}}CV$$

$$CV = \frac{1}{1+K_2\ P_{CO}\gamma_{CO}\ +2\sqrt{K_3\ \ K_2\ \gamma_{CO}\ P_{CO}}+\sqrt{K1\gamma_{H_2}P_{H_2}}}$$

Finally, we can develop genetic algorithm code to estimate the parameters (K_1, K_2, K_3, K_4, K_5, k_6, k_{par}, k_{par1}, k_{olef}, k_{olef2}, k_{pro}, c , γ_{CO}, γ_{H_2})